



A thermodynamically consistent phase transformation model for multiphase alloys: application to $\text{Ti}_6\text{Al}_4\text{V}$ in laser powder bed fusion processes

Isabelle Noll¹ · Thorsten Bartel¹ · Andreas Menzel^{1,2}

Received: 30 November 2023 / Accepted: 23 March 2024
© The Author(s) 2024

Abstract

Titan aluminium alloys belong to the group of α - β -alloys, which are used for many applications in industry due to their advantageous mechanical properties, e.g. for laser powder bed fusion (PBF-LB) processes. However, the composition of the crystal structure and the respective magnitude of the solid fraction highly influences the material properties of titan aluminium alloys. Specifically, the thermal history, i.e. the cooling rate, determines the phase composition and microstructure for example during heat treatment and PBF-LB processes. For that reason, the present work introduces a phase transformation framework based, amongst others, on energy densities and thermodynamically consistent evolution equations, which is able to capture the different material compositions resulting from cooling and heating rates. The evolution of the underlying phases is governed by a specifically designed dissipation function, the coefficients of which are determined by a parameter identification process based on available continuous cooling temperature (CCT) diagrams. In order to calibrate the model and its preparation for further applications such as the simulation of additive manufacturing processes, these CCT diagrams are computationally reconstructed. In contrast to empirical formulations, the developed thermodynamically consistent and physically sound model can straightforwardly be extended to further phase fractions and different materials. With this formulation, it is possible to predict not only the microstructure evolution during processes with high temperature gradients, as occurring in e.g. PBF-LB processes, but also the evolving strains during and at the end of the process.

Keywords Titan aluminium · Additive manufacturing · Microstructure · Material modelling · Homogenization

1 Introduction

$\text{Ti}_6\text{Al}_4\text{V}$ belongs to the group of α - β -alloys, which possess different phases with distinct crystal structures, compare Fig. 1. The chemical composition according to, e.g., DIN EN ISO 5832-3 [18] influences the volume fractions of the α - and β -phases along specific temperature paths. The α -phase is stabilised by aluminium and the β -phase is stabilised by vanadium. In addition, the β -transus temperature depends on the material composition. Especially the content of oxygen,

as well as the heat treatment define the final crystal structure of the material. The α -phase can consist of lamellar or equiaxed microstructures as well as a combination of both, see [14, 33] for further information. The lamellar structure of the α -phase can be influenced by the cooling rate or heat treatment with e.g. furnace, air, water or gas. This may result in plate-like α -, acicular α -, Widmanstaetten α -, hcp martensite α' - or in orthorhombic martensite α'' -phases. Based on the resulting microstructure, the thermal and mechanical properties of the titanium alloy differ significantly, respectively are considerably influenced. In-situ experimental validation of the microstructure during PBF-LB can be found in, e.g., [29, 56]. However, there is still a lack of comprehensive understanding of the phase transformation processes, especially for the rapid temperature cycles present in PBF-LB, which is essential to ensure adequate mechanical properties.

For PBF-LB processes, $\text{Ti}_6\text{Al}_4\text{V}$ is one of the most frequently used titanium alloys, compare DIN EN ISO/ASTM 52911-1 [2]. Therefore, consideration of the transitions

✉ Isabelle Noll
isabelle.noll@tu-dortmund.de

¹ Department of Mechanical Engineering, Institute of Mechanics, TU Dortmund University, Leonhard-Euler-Str. 5, 44227 Dortmund, Germany

² Division of Solid Mechanics, Department of Construction Sciences, Lund University, P.O. Box 118, 221 00 Lund, Sweden

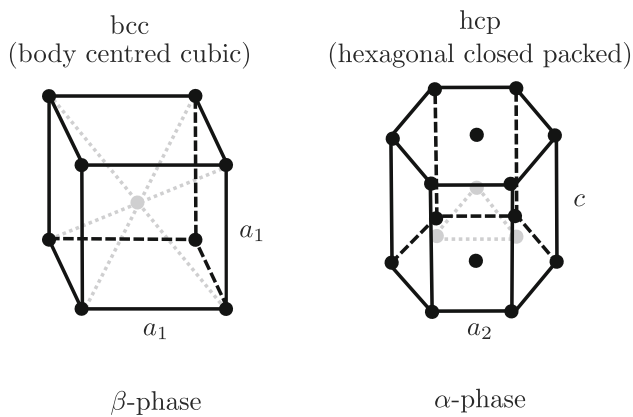


Fig. 1 Crystal structures of unit cell for β - and α -phases of $\text{Ti}_6\text{Al}_4\text{V}$ with lattice parameters $a_1 = 0.319$ nm for bcc and $a_2 = 0.2925$ nm, $c = 0.4670$ nm for hcp, cf. [14]

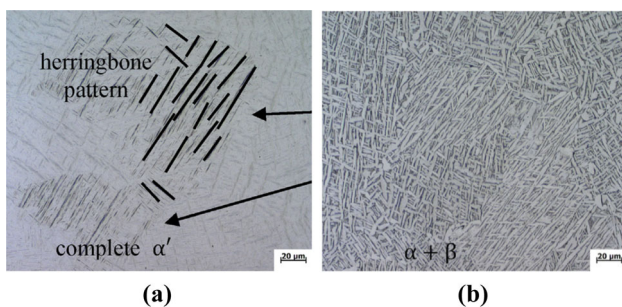


Fig. 2 In-plane microstructure of $\text{Ti}_6\text{Al}_4\text{V}$ parts manufactured by PBF-LB: **2a** as fabricated ($P = 280$ W, $v^{\text{lsf}} = 1.2$ m/s) resulting in complete α' martensite with herringbone pattern due to alternating scanning direction; **2b** heat treated at 900°C resulting in $\approx 30\%$ β -phase. Reprinted from Journal of Alloys and Compounds, 782, Liang, Z., Sun, Z., Zhang, W., Wu, S., Chang, H., The effect of heat treatment on microstructure evolution and tensile properties of selective laser melted $\text{Ti}_6\text{Al}_4\text{V}$ alloy, 1041–1048. Copyright (2019), with permission from Elsevier, [34]

between the β - and the different α -phases is of key importance for the modelling and simulation of PBF-LB processes. The temperature profiles associated with these processes, which are highly heterogeneous in space and time, further increase the complexity. Especially high heating and cooling rates (up to $10^3 - 10^8$ K/s) are characteristic during and shortly after the material is heated by the laser beam, cf. [10, 34, 40, 53]. In addition, process parameters influence the overall temperature history and thus the microstructure, resulting in fine acicular α' martensite structures, as illustrated in Fig. 2a, or in β -grain boundaries with α' martensites in-between, cf. [49, 52]. Subjacent layers and previous melt tracks exhibit significantly different temperature gradients, while low rates are present during the final cooling period. If subsequent annealing is used, a new and distinct temperature cycle is applied to the material changing the overall microstructure, compare Fig. 2b, and mechanical behaviour, cf. the experimental investigations in [34, 37, 57].

Therefore, not only TTT (time temperature transformation) diagrams, but mostly so-called CCT (continuous cooling transformation) diagrams are necessary to understand the material's behaviour and to calibrate material models. Experimental studies of $\beta \rightarrow \alpha$ phase transformation during continuous cooling can be found in, e.g., [5, 19, 25, 39, 50]. A schematic CCT diagram was first published in [5], compare Fig. 3, where the continuous cooling by using water or helium gas was monitored by thermocouples. In the previously mentioned literature, one has to distinguish between cooling curves that were actually measured on the specimen, also denoted as part, and are therefore not constant in the cooling rate $\dot{\theta}$ (see, e.g., [5, 19, 54]) and constant cooling curves (see, e.g., [25, 39]), where the prescribed constant cooling rate $\dot{\theta}$ is used to construct the CCT diagram.

In [39], experimental investigations on the time-dependent evolution of phase fractions are presented. This evolution is generally characterised by an asymptotic behaviour towards values of zero and one. Furthermore, a clear tendency towards faster transformations for higher cooling rates is shown. In addition, at slow cooling rates it is observed that the considered specimen exhibits a residual β -phase fraction of 9% in the final cooled state. In [25], it is reported that the amount of residual β -phase depends on the cooling rates ranging from 12.7% for higher cooling rates to 6.5% for lower cooling rates. The experimentally obtained results shown in [54] also confirm the occurrence of residual β -phase. An overview of different critical cooling rates and characteristic temperatures is provided in Tables 1 and 2. The state of research uniformly confirms that the morphology of the α -phase depends on the cooling rate: decreasing the cooling rate results in increased lamella, respectively grain size, whereas the morphology changes from Widmannstaetten lamellas to equiaxed grains.

Different modelling approaches can be found in the literature, most of them relying on algebraic equations for isothermal conditions based on the Johnson-Mehl-Avrami(-Kolmogorov) (JMA(K)) theory, compare [6, 26, 31] and the concept of additivity as introduced in, e.g., [39]. In addition, the Koistinen-Marburger (KM) model, see [30], is frequently used for martensitic transformations. In [62], not only the physical state changes, i.e. melting and solidification, but also the metallurgical solid-state phase transformations are incorporated. Here, the physical state changes are based on the solidus and liquidus temperatures, whereas a phenomenological approach is used for the solid-state phase transformation. To be more specific, the TTT diagram, an extended JMA model for diffusional transformations and the KM model are combined. Five different phases of $\text{Ti}_6\text{Al}_4\text{V}$ are considered in the generic parent-child framework, where the critical cooling rates are taken from [5]. For a homogeneous stress state, two different heating-cooling cycles are prescribed and the resulting microstructure is discussed. However, no predictions are made regarding the stress-strain

Fig. 3 Schematic CCT diagram for Ti₆Al₄V. At the temperature $\theta_{\beta,trans}$, the β -phase first transforms (partially) into the α -phase. Subsequently, different α -phases form depending on the temperature and cooling rate, where M_s refers to the martensitic start temperature. Reprinted from Materials Science and Engineering, 243, Ahmed, T., Rack, H., Phase transformations during cooling in $\alpha + \beta$ titanium alloys, 206–211. Copyright (1998), with permission from Elsevier, [5]

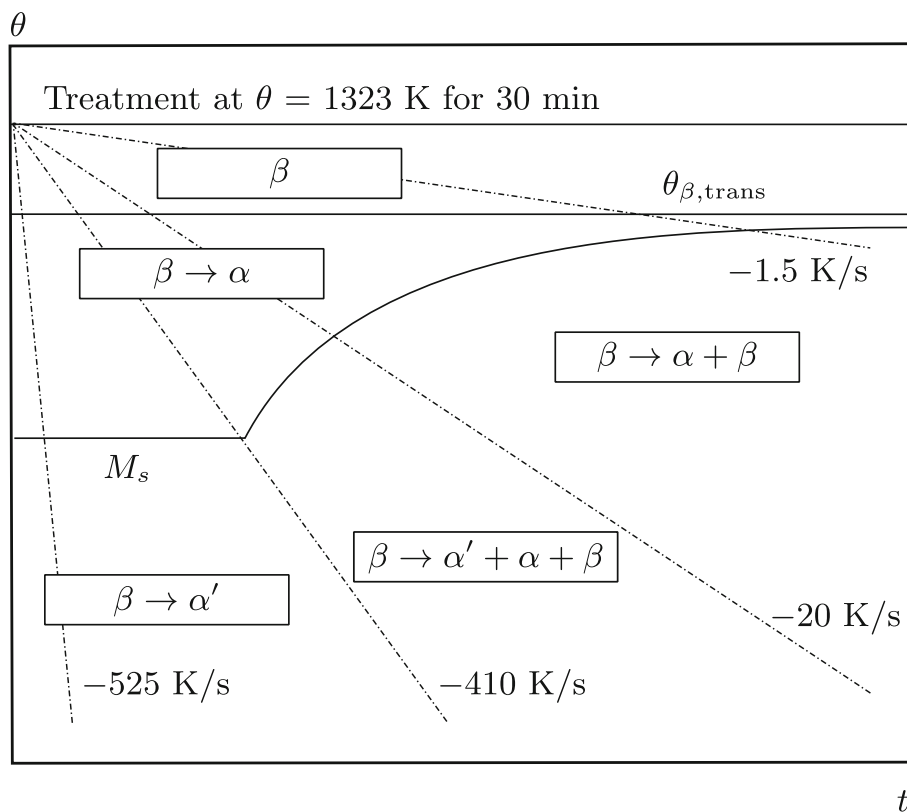


Table 1 Literature overview of critical cooling rates $\dot{\theta}$ for the different transformation possibilities

References	Diffusive $\beta \rightarrow \alpha + \beta$ (K/s)	Mixed $\beta \rightarrow \alpha' + \alpha + \beta$ (K/s)	Diffusionless $\beta \rightarrow \alpha'$ (martensitic) (K/s)
[5]	< 20	20–410	> 410
[39]	0.167–0.83	–	–
[25]	0.01–10	–	18–200
[19]	0.012–2.5	7.3	23.1

behaviour. Other recent publications in the field of additive manufacturing (AM) that are based on the JMA and KM models are, e.g., [7, 11, 22, 24, 59]. The model in [59] not only predicts the distribution of the different solid-state phases during the process and after heat treatment, but also proposes a Rosenthal-based solidification process map for PBF-LB. In [24], a visualisation of the difference and improvement in residual stress prediction incorporating martensitic phase transformations for tool steel is shown. A part-scale model coupled with the JMA equation is used in [22, 55]. In [36], the authors present an integrated simulation framework distinguishing between a thermal process model, a predictive solidification model for the molten pool and a solid-state phase transformation model for $\beta \rightarrow \alpha/\alpha'$. One of the few thermally coupled models is [11], where a process-based finite element (FE) model simulating a thin walled structure is presented. An Abaqus model is elaborated in [7], where not only the JMA and KM equation

are incorporated, but also a purely temperature driven melting and solidification. Another approach in [58] is based on a kinetics model formerly used for weld joints to predict the microstructure and hardness of high-strength steels. The model is applied sequentially to locations of interest based on the chemical composition and thermal history. However, the above described models are purely empirical. It appears that micromechanically motivated and thermodynamically consistent material models appropriately predicting stress and strain states are missing.

As an alternative, a phase field approach for the solid-state phase transformation is suggested in [3] for welds, which could also be applied to AM processes. In [35], a framework based on crystal plasticity is presented for H13 tool steel. In [10], a different approach is chosen where temperature-dependent functions are fitted to account for the different material properties of the α' - and β -phases. Therefore, the respective function of the solid phase is used

Table 2 Literature overview of characteristic temperatures during cooling: β -transus $\theta_{\beta,\text{trans}}$, martensitic start M_s and martensitic finish M_f

References	$\theta_{\beta,\text{trans}}$ (K)	M_s (K)	M_f (K)
[5]	1267	848	–
[39]	1243	–	–
[50]	1268	–	–
[25]	1243	1143	998
[19]	1243	1188	963

based on the current temperature θ and β -transus temperature $\theta_{\beta,\text{trans}}$. However, no rate dependency is incorporated. In [43], a stochastic approach is used to model the microstructure evolution during solidification. Based on the work of [5], the authors of [44] developed a phenomenological material model which captures the phase transformations during PBF-LB processes. In this contribution, the β , α , α' -phases are considered, the evolution of which are either diffusion-based or non-diffusion based. The model parameters are determined by an inverse identification process based on TTT diagram data. With this framework at hand, CCT data can be predicted with sufficient accuracy. In contrast, [60] uses the thermal history of an FE analysis to predict the microstructure evolution, i.e. phase fractions, of magnetic materials based on the software CALPHAD. With this approach, the phase fraction is estimated for the given composition and temperature using the lever rule. Similarly, in [51] the advantages using a CALPHAD based FE model rather than a standard FE model are discussed for SS316L.

A comprehensive overview of the current state of the art is given in [53], in particular with respect to continuous heating transformation (CHT) diagrams, CCT diagrams and microstructures for $\text{Ti}_6\text{Al}_4\text{V}$. Among other things, the authors point out the lack of accurate models to predict and control the microstructural evolution during AM processes and the diverse and contradicting values for significant model parameters provided in literature, compare Tables 1 and 2. The authors also propose a new concept denoted time-phase transformation-block (TPTB) to simultaneously take into account the different phase transformation mechanisms. Applications of this concept in the context of direct energy deposition (DED) are shown in [53]. The results obtained with this approach may help to adapt and improve the present JMA and KM models in the future. However, the TPTB model is rather complicated as it includes quite many parameters and, in addition, does not provide a relation between stresses and strains. More simple models are presented in [15, 17], where a phenomenological and explicit relation between the phase fractions and the present temperature as well as the cooling rate is used.

The incorporation of a framework that is capable of simulating solid-state phase transformations is important for two

reasons: the cooling rate during the manufacturing process of the part as well as possible subsequent reheating or heat treatments alter the microstructure and residual stress state of the manufactured part. This is the case, as the crystal structure and material properties of the phases differ. Therefore, especially for heat treatable alloys like $\text{Ti}_6\text{Al}_4\text{V}$, the incorporation and monitoring of solid-state phase transformation cannot be neglected, as the strongly cooling rate dependent phase composition needs to be additionally considered. The focus of the present work is set on the prediction of phase fractions during temperature-induced transformations for different temperature rates. In this context, the aim of the present contribution is to develop a material model, which is capable of simulating phase transformations between two different solid phases as well as their effect on deformation and—if incorporated into a FE approach in future—on residual stresses based on a linear elasticity analysis. The fact that the model is based on the principles of thermodynamics and appropriate homogenisation assumptions (in contrast to, e.g. [7, 11, 15, 17]) should, in principle, lead to more accurate predictions of effective quantities. This feature is specifically important for simulations of AM processes such as PBF-LB. In order to adapt the modelling framework to the complex behaviour of $\text{Ti}_6\text{Al}_4\text{V}$, a new approach with respect to the dissipation function is developed. The material parameters incorporated in the material model and, in particular, in the new dissipation function are identified using CCT curves available from the literature.

The paper is structured as follows: In Sect. 2, the general concept of the solid–solid phase transformation framework with an extended dissipation function is presented. Thereafter, the algorithmic implementation is summarised in Sect. 3, where a focus is set on the parameter identification process for the dissipation function. In Sect. 4, the reproduced CCT diagram and examples of different boundary value problems (BVP) demonstrate the capability of the model at hand. The paper closes with conclusions and a brief outlook in Sect. 5.

2 Methodology of the solid-solid phase transformation framework

The phase transformation framework, which is based on the consideration of several phases along with respective energy densities, is summarised in this section. For the current material model, three different phases are used, namely the molten phase, the solid β -phase and the solid α -phase, which are introduced in Sect. 2.1. Furthermore, the evolution equations together with the involved parameters, which are used to adapt the material behaviour of the phase transformation model for different cooling rates, are defined.

2.1 Phase energy densities

The constitutive framework used in this work is based on the model established in [45]. While focusing on the transformation from the molten to the solid phase in the present work, the framework of [45] is extended in terms of the consideration of two solid-phases, namely the β - and α -phases. As this work proceeds, no distinction between α - and α' -phases shall be made and the material behaviour in the solid phases is assumed purely elastic. However, related model extensions would be possible in a straightforward manner.

First, the phase energy density of the molten phase is introduced in a small strain setting as

$$\psi_{\text{mel}} := \frac{1}{2} [\boldsymbol{\epsilon}_{\text{mel}} - \boldsymbol{\epsilon}_{\text{mel}}^{\text{trans}}] : \mathbf{E}_{\text{mel}} : [\boldsymbol{\epsilon}_{\text{mel}} - \boldsymbol{\epsilon}_{\text{mel}}^{\text{trans}}] - c_{\text{mel}} \theta \ln(\theta) - L_{\text{mel}} \frac{\theta - \theta_{\text{mel}}^{\text{ref}}}{\theta_{\text{mel}}^{\text{ref}}}, \tag{1}$$

where $\boldsymbol{\epsilon}_{\bullet}$ refers to the total strains, \mathbf{E}_{\bullet} represents the fourth-order isotropic elasticity tensor, c_{\bullet} denotes the heat capacity, θ is the absolute temperature, and L_{\bullet} indicates the latent heat with reference temperature $\theta_{\bullet}^{\text{ref}}$ of the corresponding phase. Moreover, $\boldsymbol{\epsilon}_{\text{mel}}^{\text{trans}}$ determines the transformation strains between the solid and molten phase, which will be further specified in Sect. 2.2. The visco-elastic strain contributions considered in [45] are neglected here since these mainly evolve during the powder-melt transformation which is not taken into account in the present work. In addition, the respective energy densities of the solid phases are defined as

$$\psi_{\text{sol},\beta} := \frac{1}{2} [\boldsymbol{\epsilon}_{\text{sol},\beta} - \boldsymbol{\epsilon}_{\text{sol},\beta}^{\text{inel}}] : \mathbf{E}_{\text{sol},\beta} : [\boldsymbol{\epsilon}_{\text{sol},\beta} - \boldsymbol{\epsilon}_{\text{sol},\beta}^{\text{inel}}] - c_{\text{sol},\beta} \theta \ln(\theta) - L_{\text{sol},\beta} \frac{\theta - \theta_{\text{sol},\beta}^{\text{ref}}}{\theta_{\text{sol},\beta}^{\text{ref}}}, \tag{2}$$

$$\psi_{\text{sol},\alpha} := \frac{1}{2} [\boldsymbol{\epsilon}_{\text{sol},\alpha} - \boldsymbol{\epsilon}_{\text{sol},\alpha}^{\text{inel}}] : \mathbf{E}_{\text{sol},\alpha} : [\boldsymbol{\epsilon}_{\text{sol},\alpha} - \boldsymbol{\epsilon}_{\text{sol},\alpha}^{\text{inel}}] - c_{\text{sol},\alpha} \theta \ln(\theta), \tag{3}$$

where

$$\boldsymbol{\epsilon}_{\text{sol},\bullet}^{\text{inel}} = \boldsymbol{\epsilon}_{\text{sol},\bullet}^{\text{th}} + \boldsymbol{\epsilon}_{\text{sol},\bullet}^{\text{trans}} \tag{4}$$

determines the inelastic strain contributions of the respective solid phase. Transformation strains $\boldsymbol{\epsilon}_{\text{sol},\bullet}^{\text{trans}}$ and thermal strains $\boldsymbol{\epsilon}_{\text{sol},\bullet}^{\text{th}}$ are considered for the solid phases to take into account the shrinkage after melting and the expansion, respectively shrinkage due to the heat input, compare Sect. 2.2. Further enhancements are possible, compare [45], where visco-elasticity and plasticity are incorporated, and [46], where visco-plasticity is considered.

2.2 Specification of inelastic strains

Conservation of mass shall be fulfilled in every material point. In consequence, the mass of an infinitesimal material volume remains constant, i.e. $dm_0 = \text{const}$. Changes in volume are included by phase transitions due to different mass densities ρ_{\bullet} . Transformation strains can straightforwardly be calculated. The incorporation of volume shrinkage has been introduced and discussed in, e.g., [20]. The (infinitesimal) initial volume dV_0 is defined as

$$dV_0 = \frac{dm_0}{\rho_0}. \tag{5}$$

Here, ρ_0 represents the mass density of the initially present phase, i.e. either melt or solid- β in the present work. With this at hand, it is possible to derive the transformed volume as

$$dV_{\bullet} = \frac{dm_0}{\rho_{\bullet}} = [1 + \text{tr}(\boldsymbol{\epsilon}_{\bullet}^{\text{trans}})] dV_0, \tag{6}$$

depending on the transformation strains which are assumed to be spherical so that

$$\boldsymbol{\epsilon}_{\bullet}^{\text{trans}} = \frac{1}{3} \left[\frac{\rho_0}{\rho_{\bullet}} - 1 \right] \mathbf{I}, \tag{7}$$

with \mathbf{I} denoting the second order identity tensor. In addition, the thermal strains

$$\boldsymbol{\epsilon}_{\text{sol},\bullet}^{\text{th}} = \alpha_{\text{sol},\bullet} [\theta - \theta_{\text{sol},\bullet}^{\text{ini}}] \mathbf{I} \tag{8}$$

are included based on a standard linear heat expansion approach with the isotropic heat expansion coefficient $\alpha_{\text{sol},\bullet}$ and the respective reference temperature $\theta_{\text{sol},\bullet}^{\text{ini}}$.

2.3 Homogenisation via convexification

Based on the approach of homogenisation via energy relaxation, material models can be developed that are unconditionally thermodynamically consistent and mathematically well-posed. The basic approach stems from the modelling of martensitic phase transformations, where volume fractions and the averaged volume specific energy are used, see, e.g., [27, 48]. For the application at hand, the algorithm is formulated with respect to the mass fractions

$$\zeta_{\bullet} = \frac{dm_{\bullet}}{dm_0}, \tag{9}$$

where dm_{\bullet} corresponds to the mass contribution of phase \bullet and dm_0 to the initial mass, both referred to a material point. In consequence, the averaged mass specific energy $\bar{\psi}$ can be

introduced based on the different mass densities in the solid and molten phase, see [45] for a more detailed overview. Moreover, it is possible to relate the mass fractions ζ_\bullet to the volume fractions ξ_\bullet via

$$\zeta_\bullet = \frac{\rho_\bullet dV_\bullet}{dm_0} = \frac{\rho_\bullet \xi_\bullet dV_0}{dm_0}, \quad (10)$$

$$\Leftrightarrow \xi_\bullet = \frac{\zeta_\bullet dm_0}{\rho_\bullet dV_0}. \quad (11)$$

The overall energy $\bar{\Psi}$ is calculated via a linear mixture rule of the mass specific phases Ψ so that

$$\bar{\Psi} = \sum \zeta_\bullet \Psi_\bullet = \frac{dV_0}{dm_0} \sum \xi_\bullet \psi_\bullet, \quad (12)$$

where the relation between the volume and mass specific energy density $\psi_\bullet = \rho_\bullet \Psi_\bullet$ holds. This averaged energy density is minimised subject to the constraints of feasible mass fraction domains, i.e. $\zeta_\bullet \in \mathcal{A}$ with

$$\mathcal{A} := \{0 \leq \zeta_\bullet \leq R_\bullet^{\text{up}}, \zeta_{\text{mel}} + \zeta_{\text{sol},\beta} + \zeta_{\text{sol},\alpha} = 1\}, \quad (13)$$

and the domain of the admissible strain distributions, also denoted compatibility condition, i.e. $\mathbf{e}_\bullet \in \mathcal{E}$ with

$$\mathcal{E} = \{\zeta_{\text{mel}} \mathbf{e}_{\text{mel}} + \zeta_{\text{sol},\beta} \mathbf{e}_{\text{sol},\beta} + \zeta_{\text{sol},\alpha} \mathbf{e}_{\text{sol},\alpha} = \mathbf{e}\}. \quad (14)$$

Therein, R_\bullet^{up} defines the upper bound of the respective mass fraction \bullet , which will be discussed in Sect. 3.1. The constrained minimisation

$$C\bar{\Psi} = \inf_{\zeta_\bullet \in \mathcal{A}} \inf_{\mathbf{e}_\bullet \in \mathcal{E}} \bar{\Psi} \quad (15)$$

would result in the so-called convex hull $C\bar{\Psi}$ of $\bar{\Psi}$, which is identical to the Reuss bound. In the present approach however, only the different total strains in each phase are determined via

$$\{\mathbf{e}_\bullet\} = \arg \inf_{\mathbf{e}_\bullet \in \mathcal{E}} \bar{\Psi}. \quad (16)$$

The evolution of mass fractions is, in contrast to strains, associated with dissipation and thus treated differently as discussed in the subsequent section. In line with the hyperelastic format, stresses are determined via

$$\sigma = \frac{\partial \bar{\Psi}}{\partial \boldsymbol{\varepsilon}} = \sum \xi_\bullet \frac{\partial \psi_\bullet}{\partial \boldsymbol{\varepsilon}}. \quad (17)$$

2.4 Evolution equations

As indicated above, the evolution of volume, respectively mass fractions is associated with dissipation. According to,

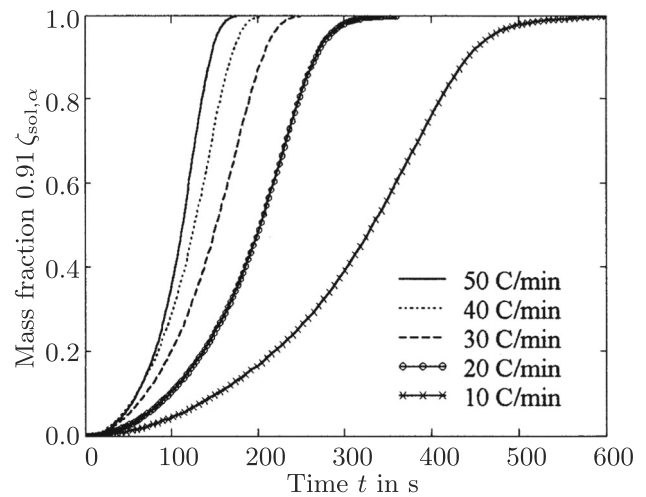


Fig. 4 Transformed mass fraction $\zeta_{\text{sol},\alpha}$ as a function of time, where a "fully" completed transformation corresponds to 91 % of $\zeta_{\text{sol},\alpha}$ and 9 % remaining $\zeta_{\text{sol},\beta}$ in the transformed state. Reprinted from Metallurgical and Materials Transactions A, 32(4), Malinov, S., Guo, Z., Sha, W., Wilson, A., Differential scanning calorimetry study and computer modeling of $\beta \rightarrow \alpha$ phase transformation in a Ti-6Al-4V alloy, 879-887. Copyright (2001), with permission from Springer Nature, [39]

e.g., [13], variational principles can be used to define

$$\frac{\partial \bar{\Psi}}{\partial \xi_\bullet} + \frac{\partial \mathcal{C}}{\partial \dot{\xi}_\bullet} = 0 \quad (18)$$

as representation of evolution equations for the variables ξ_\bullet depending on the dissipation function \mathcal{C} . Therein, notation $\dot{\bullet}$ indicates the derivative with respect to time. The first term in eq. (18) includes the so-called driving forces $\mathcal{F}_\bullet := -\partial_{\xi_\bullet} \bar{\Psi}$. In the present work, the dissipation function is chosen as

$$\mathcal{C} = \sum \dot{\bullet} Y_\bullet |\dot{\xi}_\bullet| + \frac{\eta_\bullet}{2} [\dot{\xi}_\bullet]^2 - \mathcal{C}'_\bullet(\xi_\bullet) |\dot{\xi}_\bullet|. \quad (19)$$

The coefficients $Y_\bullet \geq 0$ and $\eta_\bullet \geq 0$ can be interpreted as a threshold Y_\bullet where the phase transformation is initiated, and as a viscosity-like parameter η_\bullet that influences the range of the (rate dependent) phase transformation. For further insight into these parameters, the interested reader is referred to [9]. The additional term $\mathcal{C}'_\bullet(\xi_\bullet)$ is here defined as

$$\mathcal{C}'_\bullet(\xi_\bullet) = a_{\bullet 1} \xi_\bullet + a_{\bullet 2} \xi_\bullet^2 + a_{\bullet 3} \xi_\bullet^3 \quad (20)$$

and adopted from [9], where bainitic phase transformations are considered. As shown in [39], Ti₆Al₄V behaves quite similarly to bainite in terms of the evolution of phase fractions, in particular for slow cooling rates, as visualised in Fig. 4; see also Remark 1. The coefficients Y_\bullet , η_\bullet , $a_{\bullet 1}$, $a_{\bullet 2}$ and $a_{\bullet 3}$ significantly affect the material behaviour. Therefore, special attention will be paid to the determination of these coefficients in Sect. 3.3.

With the specific choice for the dissipation function at hand, the evolution equation introduced in eq. (18) for each phase fraction is in general given by

$$-\mathcal{F}_\bullet + [Y_\bullet - C'_\bullet(\xi_\bullet)] \text{sign}(\dot{\xi}_\bullet) + \eta_\bullet \dot{\xi}_\bullet = 0 \tag{21}$$

leading to

$$\dot{\xi}_\bullet = \frac{1}{\eta_\bullet} \langle |\mathcal{F}_\bullet| - Y_\bullet + C'_\bullet(\xi_\bullet) \rangle \text{sign}(\mathcal{F}_\bullet) , \tag{22}$$

where

$$\langle \bullet \rangle = \max \{ \bullet, 0 \} \tag{23}$$

refers to the Macaulay brackets. As discussed in [9], the non-standard format of the dissipation function requires the investigation of thermodynamic consistency. In this context, it must be shown that

$$C \geq 0 , \tag{24}$$

which is satisfied for

$$Y_\bullet - C'_\bullet(\xi_\bullet) \geq 0 \Leftrightarrow C'_\bullet(\xi_\bullet) \leq Y_\bullet \tag{25}$$

since $\eta_\bullet \geq 0$. This condition is always fulfilled if

$$C'_{\bullet\max} := C'_\bullet(\xi_{\bullet\max}) \leq Y_\bullet \tag{26}$$

with

$$\xi_{\bullet\max} = \frac{-a_{\bullet 2} - \sqrt{-c_{\bullet 1}}}{3 a_{\bullet 3}} \tag{27}$$

and

$$c_{\bullet 1} := -a_{\bullet 2}^2 + 3 a_{\bullet 3} a_{\bullet 1} . \tag{28}$$

In conclusion, two inequality constraints are derived, namely

$$c_{\bullet 1} := -a_{\bullet 2}^2 + 3 a_{\bullet 3} a_{\bullet 1} \leq 0 \tag{29}$$

and

$$c_{\bullet 2} := a_{\bullet 3} \xi_{\bullet\max}^3 + a_{\bullet 2} \xi_{\bullet\max}^2 + a_{\bullet 1} \xi_{\bullet\max} - Y_\bullet \leq 0 . \tag{30}$$

These conditions, i.e. eqs. (29) and (30), have to be implemented into the parameter identification process, which will be discussed in Sect. 3.3.

Remark 1 In [9], an approach for phase transformations is developed to reproduce the temporal behaviour of bainite. Based on this, an extension of the evolution equation to model the characteristic material behaviour of bainite is

sought, which is suitable for the modelling of the rate dependent behaviour of titan aluminum alloy, compare Fig. 4. This means that changing velocities, respectively rates, of solid mass fractions during the phase transformation (from small to large to small), as well as changing accelerations, respectively the time derivative of the rates, (from positive to negative) have to be captured by the dissipation function. As a result, the cubic polynomial in ξ_\bullet has been proposed as a dissipation function contribution in [9], see eq. 20.

For the present phase transformation framework, it is assumed that the additional term (20) acts as a fully dissipative contribution. Therefore, C'_\bullet is added to eq. (19) and acts as an additional threshold contribution to the yield limit Y . However, as discussed in [9], it is also possible to assign this contribution to the energy by using an additional surface-type energy density $\psi_\bullet^{\text{surf}} = -\int C'_\bullet d\xi_\bullet$, which is added to the corresponding phase energy density. This can be interpreted as a contribution related to the interaction between the different phases, which is not accounted for within the standard energy density of the bulk material. By using a weighting factor, it is possible to allocate C'_\bullet as a contribution to either energy density or dissipation function or a combination of both.

3 Algorithmic implementation

In general, the solution of eq. (22) determines the phase fractions of the material and with it the predicted material behaviour. Due to the variational nature of the problem, the associated constraints can be incorporated by using, e.g., smoothed Fischer-Burmeister nonlinear complementarity functions, and standard solvers such as the Newton–Raphson scheme can be applied. For further insight into the implementation and the calculation of the phase fractions and residual strains, respectively stresses, the interested reader is referred to [45]. In the following, some specific aspects of the algorithmic implementation shall be addressed for the melt-solid-solid phase transformation.

3.1 Case differentiation

In general, the consideration of several and potentially co-existing phases is possible, compare [8], but may become challenging in view of numerical stability and especially efficiency. The goal of this section is to show as to how the implementation can significantly be simplified by case differentiation. In general, the specimen is molten above the melting point $\theta^{\text{melt}} = \theta_{\text{mel}}^{\text{ref}} = 1873.15$ K. As discussed in Sect. 1, Ti₆Al₄V completely consists of the β -phase above the β -transus temperature, cf. Figure 3. Depending on the initial temperature, the reference state is either $\zeta_{\text{mel}} = 1$ or $\zeta_{\text{sol},\beta} = 1$. Only below the temperature $\theta_{\beta,\text{trans}}$, the β -phase

(partially) transforms into further phases, where the focus is here laid on the α -phase as indicated above, while α' is so far neglected. Due to the physical behaviour of the titanium alloy, it is possible to consider only two phases at the same time, which simplifies the related model, respectively mathematical problem. Therefore, several sets of variables along with corresponding constraints need to be defined and considered within the model. In view of the melt \rightarrow solid- β transformation, constraints

$$\{\zeta_{\text{mel}}, \zeta_{\text{sol},\beta}\} \in \mathcal{A}_1 \quad , \quad \{\mathbf{e}_{\text{mel}}, \mathbf{e}_{\text{sol},\beta}\} \in \mathcal{E}_1 \quad (31)$$

with

$$\mathcal{A}_1 := \{0 \leq \zeta_{\text{sol},\beta} \leq 1, \zeta_{\text{mel}} + \zeta_{\text{sol},\beta} = 1\} \quad (32)$$

and

$$\mathcal{E}_1 = \{\zeta_{\text{mel}} \mathbf{e}_{\text{mel}} + \zeta_{\text{sol},\beta} \mathbf{e}_{\text{sol},\beta} = \mathbf{e}\} \quad (33)$$

are introduced. Subsequently, the sets

$$\{\zeta_{\text{sol},\beta}, \zeta_{\text{sol},\alpha}\} \in \mathcal{A}_2 \quad , \quad \{\mathbf{e}_{\text{sol},\beta}, \mathbf{e}_{\text{sol},\alpha}\} \in \mathcal{E}_2 \quad (34)$$

with

$$\mathcal{A}_2 := \left\{1 - R_{\text{sol},\alpha}^{\text{up}} \leq \zeta_{\text{sol},\beta} \leq 1, \zeta_{\text{sol},\beta} + \zeta_{\text{sol},\alpha} = 1\right\} \quad (35)$$

and

$$\mathcal{E}_2 = \{\zeta_{\text{sol},\beta} \mathbf{e}_{\text{sol},\beta} + \zeta_{\text{sol},\alpha} \mathbf{e}_{\text{sol},\alpha} = \mathbf{e}\} \quad (36)$$

are used for the solid- $\beta \rightarrow$ solid- α transformation, where $R_{\text{sol},\alpha}^{\text{up}}$ is the upper bound for the α -phase. Experiments show that the maximum value of the α -phase does not necessarily has to take value one and depends mainly on the given cooling rate. More precisely speaking, the results presented in, e.g., [25, 39, 54] show that this holds for relatively slow cooling rates. Based on these observations, the assumption

$$R_{\text{sol},\alpha}^{\text{up}} = \begin{cases} 1.00 \rightarrow \zeta_{\text{sol},\alpha}, & \text{for high } |\dot{\theta}| \\ 0.95 \rightarrow \zeta_{\text{sol},\alpha}, & \text{for medium } |\dot{\theta}| \\ 0.90 \rightarrow \zeta_{\text{sol},\alpha}, & \text{for low } |\dot{\theta}| \end{cases} \quad (37)$$

is made in the present model. The values for medium and low cooling rates are approximated based on available literature data. The model relies in particular on the results presented in [5], see also Remark 2. This leads to the definitions

$$\begin{aligned} \text{high:} & \quad 410 \text{ K/s} < |\dot{\theta}| \\ \text{medium:} & \quad 20 \text{ K/s} \leq |\dot{\theta}| \leq 410 \text{ K/s} \\ \text{low:} & \quad |\dot{\theta}| < 20 \text{ K/s} \end{aligned} \quad (38)$$

for the temperature rates. Moreover, the equality constraints in eq. (32) and (35) allow for the substitutions

$$\zeta_{\text{mel}} = 1 - \zeta_{\text{sol},\beta} \quad \text{or} \quad \zeta_{\text{sol},\alpha} = 1 - \zeta_{\text{sol},\beta} \quad , \quad (39)$$

so that in both cases only one mass fraction is used as variable. With this, the general approach introduced in eq. (19) simplifies to one summand, i.e. only one independent mass fraction remains for the particular case considered, cf. eqs. (31, 34, 39). Thus, no distinction between coefficients related to different phases in the dissipation function \mathcal{C} is necessary as this work proceeds.

In addition, it is possible to consider cooling from melting or cooling from the β -phase. In view of the parameter identification approach discussed in Sect. 3.3, only solid- $\beta \rightarrow$ solid- α transformation is considered. For the PBF-LB process, all three phases are present. This results in an adjustment of the initial composition of the material, i.e. ζ_{\bullet} and mass density ρ_0 , cf. Sect. 2.2. Moreover, the respective transformation strains according to eq. (7) have to be adapted in terms of the reference mass density ρ_0 . In conclusion, based on the particular process, e.g. heat treatment or AM, one may either start with cooling from the molten phase, so that $\theta^{\text{start}} > \theta_{\text{mel}}^{\text{ref}}$, or with $\theta_{\text{mel}}^{\text{ref}} > \theta^{\text{start}} > \theta_{\text{sol},\beta}^{\text{ref}}$, where the initial material composition lies purely within the β -phase. A consecutive heating and additional cooling of the material is also captured by the implementation.

Remark 2 As summarised in Table 1 and also stated in the literature, see e.g. [53, 54], the explicit values chosen for the critical rates, martensitic start temperature and maximum values vary significantly. The model at hand can straightforwardly be adapted to new experimental results, so that one could use improved maximum values for the phase fractions and critical cooling rates. It would therefore be possible to determine more reliable parameters for the dissipation function, see Sect. 3.3.

3.2 Stress-free states

In order to evaluate the material response of the present framework, the behaviour under stress-free boundary conditions shall be analysed. Within the proposed material model, the constitutive relation for the stresses is highly non-linear in terms of strains and temperature. This, in general, requires an iterative computational approach to solve for the unknown quantities. As this work proceeds, such algorithm shall be denoted as constitutive driver, cf. Algorithm 1. Within this constitutive driver, different types of temperature evolution, i.e. cooling and heating profiles $\bar{\theta}(t)$ depending on time t , are prescribed at material point level. Accordingly, one sees the strain state \mathbf{e}_n for the prescribed temperature path $\bar{\theta}(t)$ at a particular instant in time t_n with prescribed temperature $\bar{\theta}_n$ and temperature rate $\dot{\bar{\theta}}_n$ which results in $\boldsymbol{\sigma}_n = \mathbf{0}$. The

Algorithm 1: Constitutive driver-temperature-induced stress-free transformations

```

Initialisation of strains  $\boldsymbol{\epsilon}_{n=0} = \mathbf{0}$  and internal variables  $\mathcal{V}_{n=0}$ 
for  $n = 1$  : steps
  Set iteration index  $i = 1$ , strains  $\boldsymbol{\epsilon}_n^1 = \boldsymbol{\epsilon}_{n-1}$ , and internal
  variables  $\mathcal{V}_n^1 = \mathcal{V}_{n-1}$ 
  while  $\|\boldsymbol{\sigma}_n^i(\boldsymbol{\epsilon}_n^i, \bar{\theta}_n, \dot{\theta}_n, \mathcal{V}_n^i)\| > \text{tol}$ 
    Compute constitutive relations and tangent
     $\{\boldsymbol{\sigma}_n^i, \mathbf{E}_n^i, \mathcal{V}_n^i\}$  based on  $\{\boldsymbol{\epsilon}_n^i, \bar{\theta}_n, \dot{\theta}_n, \mathcal{V}_{n-1}^i\}$ 
    Update of strains
     $\boldsymbol{\epsilon}_n^{i+1} = \boldsymbol{\epsilon}_n^i - [\mathbf{E}_n^i]^{-1} : \boldsymbol{\sigma}_n^i$ 
    Update of iteration index
     $i \leftarrow i + 1$ 
  end while
  Save strains  $\boldsymbol{\epsilon}_n = \boldsymbol{\epsilon}_n^i$  and internal variables  $\mathcal{V}_n = \mathcal{V}_n^{i-1}$ 
end for

```

determination of strains includes the calculation of internal variables

$$\mathcal{V}_n = \mathcal{V}(\boldsymbol{\epsilon}_n, \bar{\theta}_n, \dot{\theta}_n) = [\zeta_{\text{mel}}, \zeta_{\text{sol},\alpha}, \zeta_{\text{sol},\beta}]_n, \tag{40}$$

where index n refers to the current time step. In summary, the relation

$$\boldsymbol{\sigma}_n(\boldsymbol{\epsilon}_n, \bar{\theta}_n, \dot{\theta}_n, \mathcal{V}_n) = \mathbf{0} \tag{41}$$

needs to be solved using, e.g., a Newton–Raphson scheme. Herein, the stresses $\boldsymbol{\sigma}_n$ are evaluated based on eq. (17). A sketch of the related constitutive driver with its most important equations is summarised in Algorithm 1. Therein, $\mathbf{E}^{\text{algo}} \approx \mathbf{E} = \partial_{\boldsymbol{\epsilon}} \boldsymbol{\sigma}$ denotes the algorithmic tangent operator, here approximated by underlying isotropic elasticity tensors.

3.3 Parameter identification

A classic parameter identification (PI) framework, as introduced in e.g. [12, 38], is used to determine suitable values for the material parameters at hand. The PI is based on the transformation behaviour as discussed in Sect. 3.1, so that all previously introduced model simplifications can be applied. As this work proceeds, a subset $\boldsymbol{\kappa} = \{Y, \eta, a_1, a_2, a_3\}$ of the underlying model parameters shall be considered within the PI, whereas the remaining model parameters are prescribed, respectively taken from literature. This means that the PI design variables or material parameters $\boldsymbol{\kappa}$, are used to sufficiently match the material response of the simulation $\mathcal{R}^{\text{sim}}(\boldsymbol{\kappa})$ to the available experimental data \mathcal{R}^{exp} . Thus, a phenomenological relation can be established between the material parameters $\boldsymbol{\kappa}$ and the cooling rate $\dot{\theta}$. For the particu-

lar cooling rates, $\zeta_{\text{sol},\alpha}$ as predicted by the proposed model is compared to the related pairs of points of the CCT diagram published in [44]. The two datasets are explicitly compared at all points in time t_n considered. Therefore, the values in between the extracted points and the maximum value $R_{\text{sol},\alpha}^{\text{up}}$ of $\zeta_{\text{sol},\alpha} = \{0.01, 0.05, 0.15, 0.45, 0.55, 0.85, R_{\text{sol},\alpha}^{\text{up}}\}$ are computed via linear interpolation, as only these discrete values can be directly extracted from [44, Fig. 6].

The overall framework corresponds to an inverse problem, whereby the least squares functional

$$f(\boldsymbol{\kappa}) = \sum_{i=1}^{n_t} \frac{1}{2} [\mathcal{R}_i^{\text{sim}}(\boldsymbol{\kappa}) - \mathcal{R}_i^{\text{exp}}]^2 \tag{42}$$

is used as objective function, where n_t denotes the number of time points considered. The dataset $\mathcal{R}_i^{\text{sim}}(\boldsymbol{\kappa})$ is calculated with the help of the constitutive driver presented in Sect. 3.2 for the given cooling rate. The optimal values for $\boldsymbol{\kappa}$ are determined by minimising $f(\boldsymbol{\kappa})$. This procedure is repeated for all temperature rates as discussed in the next Sect. 3.4.

Prior to the use of $\boldsymbol{\kappa}$ within the constitutive driver the related inequality constraints (28) and (30) are checked. In the case where these constraints are violated, the respective design variables are set to the related limit values. The gradient free fminsearch-algorithm (a Nelder–Mead simplex algorithm) available within the commercial software MATLAB is used for the PI by minimising the objective function defined in eq. (42). The thermodynamic consistency constraints (29) and (30) are checked after the PI is performed and, for the applications considered in this work, always turned out to be satisfied. As no general proof can be established for the determination or existence of the global minimum of the underlying least squares functional, multiple local minima are to be expected. Thus, a set of different initial values of the design variables $\boldsymbol{\kappa}$ is used. Conceptually speaking, a (coarse) grid search approach is applied to identify different minima for $\boldsymbol{\kappa}$. Sect. 4.1 discusses how the values between the identified points are approximated.

3.4 Summary of complete workflow

For the present modelling framework, 18 cooling curves with the respective material composition are extracted from the CCT diagram published in [44]. In line with experiments, the temperature profiles are not assumed to be linear functions in time. Rather, the calculated temperature-time curves depicted in Fig. 5 are used, see also Remark 3. The procedure for generating the temperature profiles is described in detail in Appendix 1. It is obvious that the cooling rate is generally not constant in time. In order to introduce a representative value for the particular cooling rate, the slope of these curves at temperature 1173 K is used. This results in the following

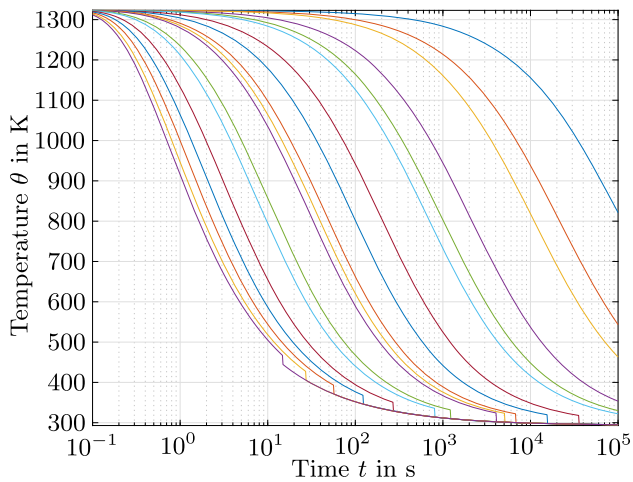


Fig. 5 Temperature profiles generated with the numerical approach presented in Appendix 1 and in [44]

cooling rates

$$\dot{\theta} = \{0.01, 0.05, 0.1, 0.5, 1, 1.5, 5, 10, 20, 25, 30, 75, 100, 200, 300, 410, 525, 600\} \text{ K/s} . \quad (43)$$

The temperature-time curves are then used as input for the constitutive driver. For all of these cooling rates the optimal design variables κ are determined with the help of the PI approach introduced in Sect. 3.3. With this framework at hand, it is possible to generate a complete CCT diagram by varying a cooling rate related scaling parameter s_g , cf. Appendix 1. Based on this, e.g., 100 cooling rates between $0.01 \text{ K/s} < \dot{\theta} < 600 \text{ K/s}$ are generated. Within the framework, the respective set of design variables κ is chosen and interpolated according to the prescribed cooling rate. The distribution of the design variables as well as the complete CCT diagram is the subject of the next section, where different boundary value problems are also discussed.

Remark 3 The temperature drops in Fig. 5 arise from the structure of the analytical solution since eq. (47), see Appendix 1, approaches infinity for some values of t and s_g , while eq. (49) takes value zero. For these cases, only eq. (48) contributes to the calculation of the temperature profile, resulting in a non-smooth curve.

4 Results

The results of the phase transformation framework are presented in the following. The mechanical and thermal material parameters used for the titanium alloy $\text{Ti}_6\text{Al}_4\text{V}$ are summarised in Table 3.

Table 3 Summary of the $\text{Ti}_6\text{Al}_4\text{V}$ material parameters used for the phase transformation framework, adapted from [10, 41]

Material parameters	Melt	Solid- β	Solid- α
<i>Mechanical parameters</i>			
Density ρ (kg/m ³)	3800	4420	4420
Poisson's ratio ν (–)	0.45	0.33	0.33
Young's modulus E (GPa)	10^{-9}	10	109
<i>Thermal parameters</i>			
Expansion coefficient α (1/K)	–	$13\text{e}-06$	$11\text{e}-06$
Initial temperature θ^{ini} (K)	–	1873.15	1873.15
Heat capacity c (J/kgK)	750	750	750
Latent heat L (kJ/kg)	286	48	–
Reference temperature θ^{ref} (K)	1873.15	1268.15	–

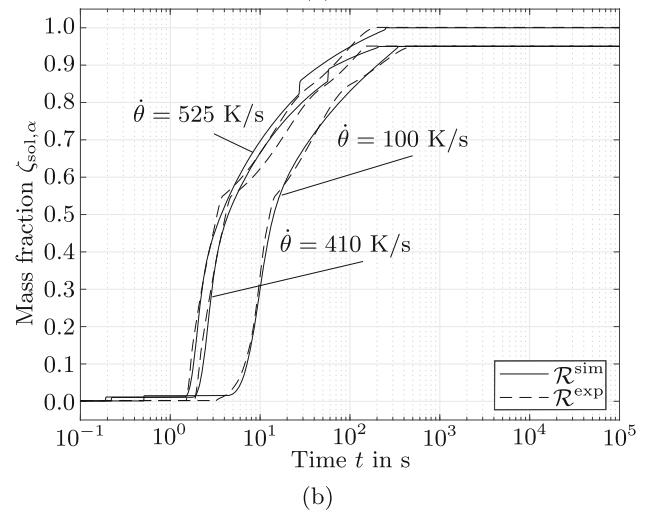
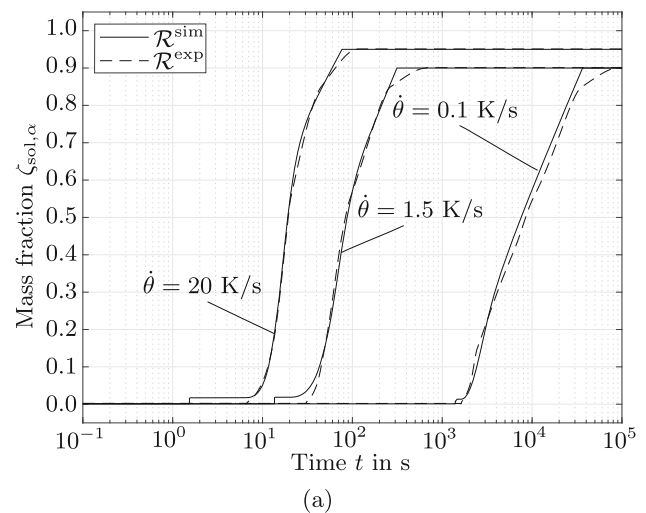


Fig. 6 Exemplary verification of calculated material response $\mathcal{R}^{\text{sim}}(\kappa)$ based on experimental data \mathcal{R}^{exp} used for the PI considering rather steady cooling rates, Fig. 6a, and rapid cooling rates Fig. 6b

4.1 Fitting of dissipation function parameters

Depending on the respective starting points for the minimisation of the objective function, different results are determined for the material parameters κ , which also yield different values for the minima of the objective function. Obviously, the objective function exhibits several local minima. However, the selection of the parameters that resulted in the lowest values of the objective function in each case led to non-smooth progressions of the phenomenological correlations $\kappa(\dot{\theta})$. In terms of numerical stability when using these correlations in finite element simulations, this should be avoided. Therefore, parameter sets κ were partly selected which did not yield the smallest value of the objective function (and yet corresponded to a local minimum), but ensured a rather smooth function $\kappa(\dot{\theta})$.

Time discrete values for the experimental curve \mathcal{R}^{exp} are taken from [44], whereas the simulation results of $\zeta_{\text{sol},\alpha}$ exemplarily depicted in Fig. 6 are generated via interpolation, as discussed in Sect. 3.3. Therein, six different curves are exemplarily chosen in order to highlight the accuracy of the results. The results for the prescribed fast, intermediate and slow cooling rates are visualised in Fig. 6, where the concentration of the α -phase, i.e. the mass fraction $\zeta_{\text{sol},\alpha}$, is plotted over time. The comparison of Fig. 6a and Fig. 6b clearly shows the influence of the prescribed cooling rate on the effective material composition. With the exception of some significant deviations for the two highest cooling rates, the results obtained with the present framework show satisfactory agreement with the experimental results. Here, the cubic polynomial \mathcal{C}' cannot fully capture the course of the experimental curves. However, the approximation is considered sufficient for the current fundamental study. In addition, the need to choose different maximum values for the mass fraction $\zeta_{\text{sol},\alpha}$ depending on the cooling rate becomes evident. The values of the parameters in the subset κ obtained by the PI depend on the cooling rate $\dot{\theta}$ via interpolation of the specific data points. Other approaches are also feasible, cf. Remark 4. These phenomenological relations are illustrated in Fig. 7. For the viscosity parameter η shown in Fig. 7a, a steep descent is visible for slow cooling rates, whereas the slope changes and decreases for higher cooling rates. For both, the threshold Y highlighted in Fig. 7b and the parameters a_1, a_2, a_3 visualised in Fig. 7c, (quasi-) constant values are generated below $\dot{\theta} < 1$ K/s, specifically $a_1 = -0.002$, $a_2 = -0.007$, $a_3 = -0.004$ GPa and above $\dot{\theta} > 525$ K/s, in particular $a_1 = 0.033$, $a_2 = -0.0621$, $a_3 = 0.009$ GPa. In between, the cooling rates significantly affect the phase changes and the temporal evolution of mass fractions. Thus, the parameters κ of the dissipation function change accordingly in order to capture the correct material response.

As there is a rather weak basis for CHT diagrams in the literature, the parameters of the dissipation function for re-

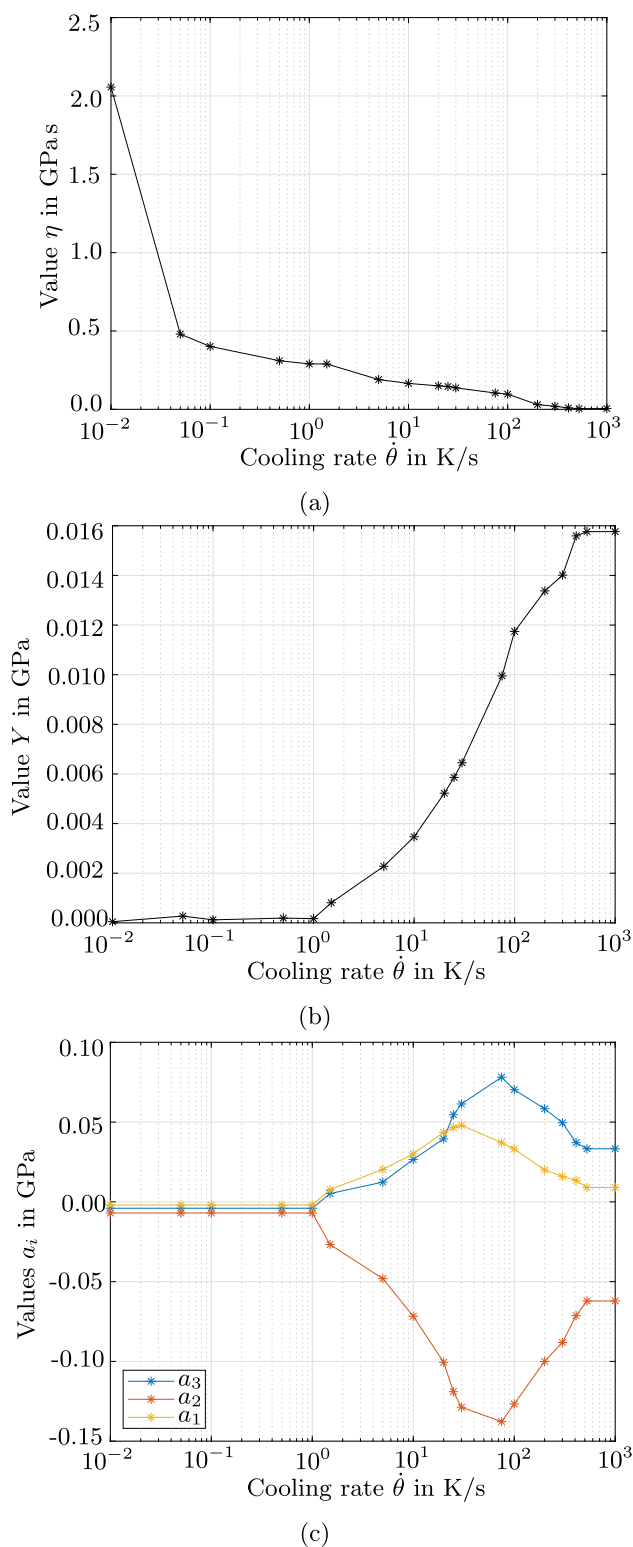


Fig. 7 Identified curves for parameters in dissipation function \mathcal{C} : parameter η as introduced in eq. (19), Fig. 7a, parameter Y as introduced in eq. (19), Fig. 7b, and parameters a_1, a_2, a_3 as introduced in eq. (20), Fig. 7c

heating are not fitted to experiments. Therefore, only the standard dissipation function is used, so that a_1 , a_2 and a_3 are set to zero a priori. The remaining parameters Y and η are identified by a trial and error process to reproduce the material behaviour and to appropriately reflect the material's transformation properties such that solid- α exists below $\theta_{\beta,\text{trans}}$ and solid- β emerges above $\theta_{\beta,\text{trans}}$. This results in the following case differentiation

$$\{\eta, Y\} = \begin{cases} \{100 \text{ GPa s}, 500 \text{ GPa}\} & \text{for } \theta < \theta_{\beta,\text{trans}} \\ \{0 \text{ GPa s}, 0 \text{ GPa}\} & \text{else} \end{cases} \quad (44)$$

These parameters cause a phase transformation to the β -phase only above the β -transus temperature $\theta_{\beta,\text{trans}}$.

For the phase transformation from molten to the β -phase, only the standard dissipation potential is used, as no complex phase transformation behaviour is assumed. The following parameters are identified in a trial and error process to ensure melting in the range of θ^{melt} ,

$$\{\eta, Y\} = \left\{ \frac{2 \text{ K/s}}{\dot{\theta}} \text{ GPa s}, 0 \text{ GPa} \right\}, \quad (45)$$

whereas $\eta = 0 \text{ GPa s}$ for $\dot{\theta} = 0 \text{ K/s}$ within the examples considered in the present work. According to our results, the rate dependence of η implies that the transformation from molten to the β -phase always starts and ends at the approximate same temperature.

Remark 4 For the current framework, the identified values of the subset $\kappa = \{Y, \eta, a_1, a_2, a_3\}$ are interpolated based on the cooling rate. Thus, a piece-wise linear relation in $\dot{\theta}$ of the

specified values is assumed. A more sophisticated approximation is possible by using a regression model based on, e.g., a least squares approach. A more elaborated approach would be the direct identification of the coefficients of smooth functions. In a next step, the current results could be used as a basis to develop a PI algorithm that determines the coefficients of, e.g., exponential, hyperbolic tangens and piecewise linear functions for all temperature rates simultaneously.

4.2 CCT diagram

With the presented rate dependent parameters it is now possible to generate a complete CCT diagram for $\text{Ti}_6\text{Al}_4\text{V}$. Therefore, the parameter s_g in eq. (50) is varied so that 100 logarithmic spaced curves are generated. The related cooling rates vary between $0.01 \text{ K/s} \leq \dot{\theta} \leq 600 \text{ K/s}$ and the resulting CCT diagram is illustrated in Fig. 8. Within this Figure, the isolines for different α -concentrations $\zeta_{\text{sol},\alpha}$ are shown. The computed CCT diagram is capable of predicting different α -fractions. The evolution of mass fractions significantly depends on the cooling rate and is highly nonlinear in time, in particular for medium cooling rates. Thus, the phase transformation begins and ends at distinct temperatures. For slow cooling rates, with $\dot{\theta} < 20 \text{ K/s}$, and high cooling rates, with $\dot{\theta} > 400 \text{ K/s}$, almost constant martensitic start temperatures M_s are present.

These general characteristics of the CCT diagram have been documented in the experimental findings of [5, 19, 25], whereas values characteristic for the transformation process, such as those summarised in Table 1 and 2, differ in literature. Since the curves given in [44] (which correspond to the

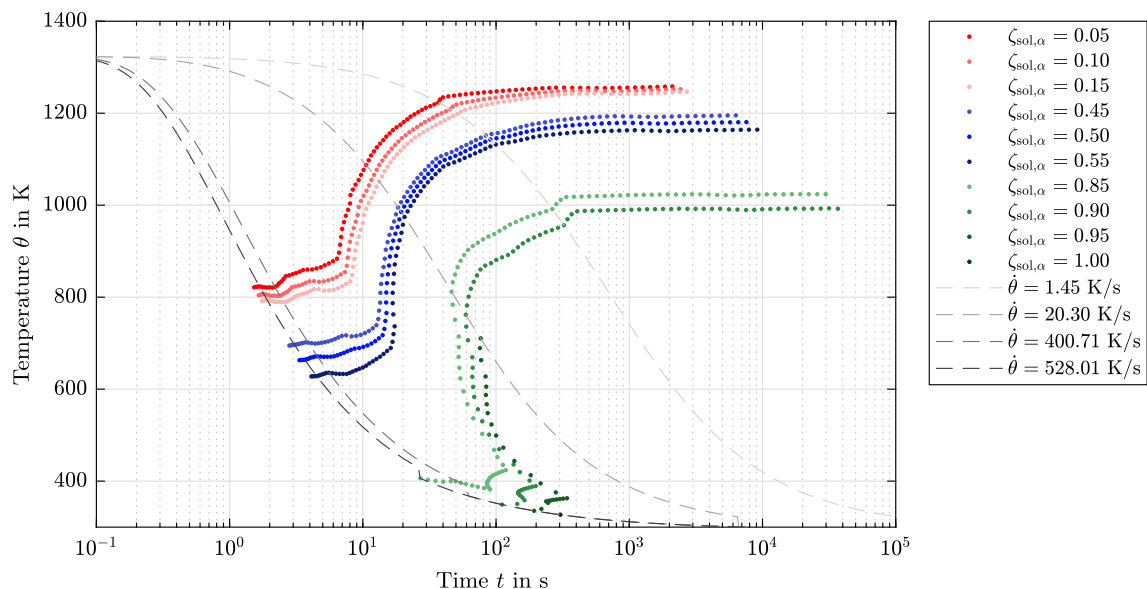


Fig. 8 Computed CCT diagram for 100 cooling rates from $\dot{\theta} = 0.01 \text{ K/s}$ to $\dot{\theta} = 600 \text{ K/s}$, where different mass fractions $\zeta_{\text{sol},\alpha}$ for the respective cooling rates are visualised. Exemplarily, four characteristic cooling rates $\dot{\theta}$ according to Fig. 3 are plotted in the CCT diagram

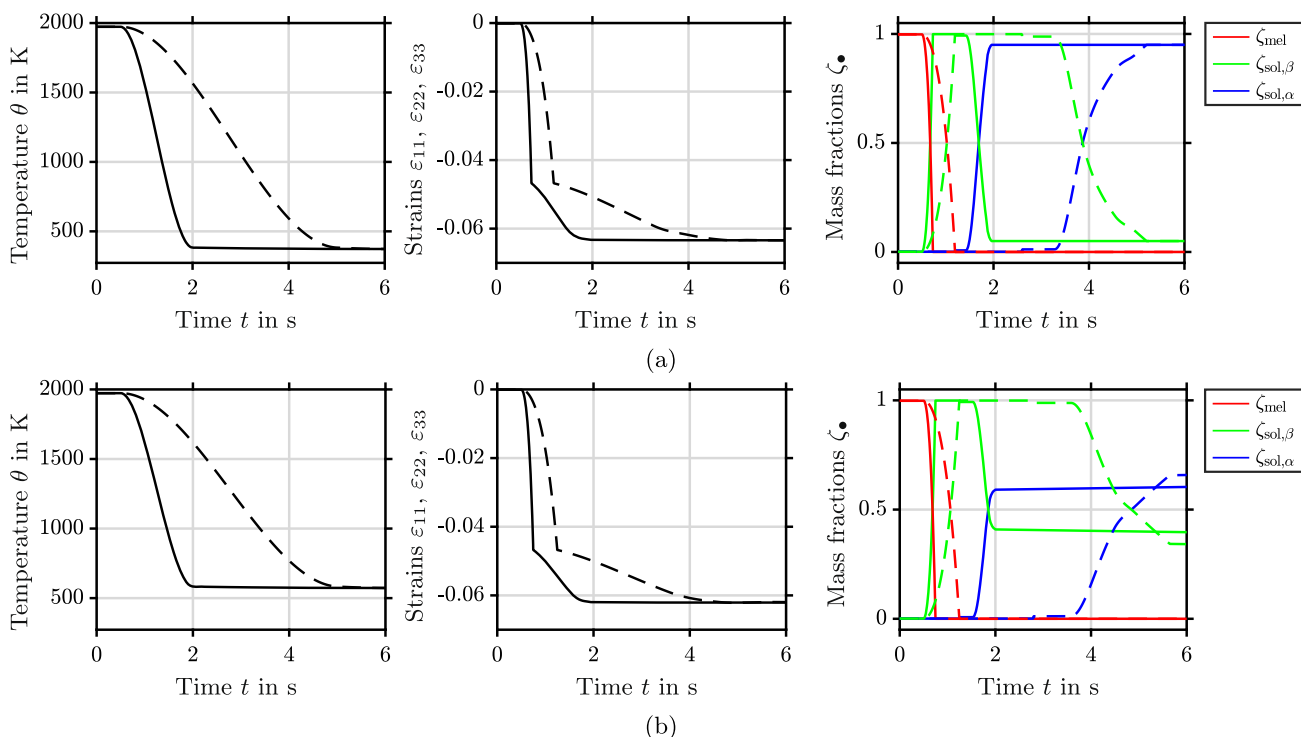


Fig. 9 Temporal evolution of homogeneous strains $\epsilon_{\bullet\bullet}$ and mass fractions ζ_{\bullet} for the high (solid lines) and low (dashed lines) cooling rate. The upper and lower figures differ from each other in terms of the final temperatures, which are precisely given by 373 K, Fig. 9a, and 573 K, Fig. 9b

experimental results of the schematic CCT diagram in [5]) are used to identify the material parameters in the present work, the agreement between these and the present results is sufficiently accurate. More precisely speaking, a β -transus temperature between 1250–1255 K is obtained, which is close to $\theta_{\beta,trans} = 1268.15$ K found in literature, cf. Table 2. A martensitic start temperature $M_s \approx 820$ K is present for fast cooling rates, which agrees with the findings in [5, 44]. However, the present model, and with it the predicted results, also takes into account the upper bound of $\zeta_{sol,\alpha}$ depending on the applied cooling rate, cf. eq. (37). The lower bound for slow cooling rates has a value of $\zeta_{sol,\alpha} = 0.85$ and lies around 400 K, which corresponds to the results in [44].

4.3 Boundary value problems

First, academic examples with simple prescribed temperature profiles are discussed as a proof of concept for the proposed framework. Thereafter, temperature profiles extracted from realised PBF-LB simulations, cf. [46, 47], are subsequently used to illustrate the explicit phase transformation of the solid for real process-based examples.

4.3.1 Proof of concept

In Fig. 9, different temperature profiles characterised by different cooling rates (high and low) as well as final tem-

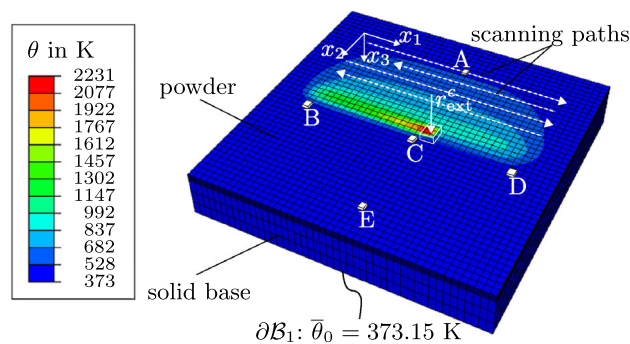


Fig. 10 Scan island simulation (characteristic scan island length 5×5 mm) with the current temperature profile at $t = 0.08$ s due to cuboid heat source r_{ext}^c with laser power $P = 250$ W and laser velocity $\bar{v}^{lsr} = 1.0$ m/s from which the temperature history $\bar{\theta}$ is extracted for elements A–E

peratures (373 K vs. 573 K) are prescribed, whereby the corresponding simulated strain and mass fraction evolution over time t is visualised. For all examples, the temperature starts above the melting point and the initial material state corresponds to completely molten material. Due to the simpler dissipation ansatz of the transformation molten \rightarrow solid- β , the transformation starts at the same temperature. Based on the cooling rate, the phase transformation takes places during different time periods. The phase change solid- $\beta \rightarrow$ solid- α is initiated at a later point of time for a slower cooling rate. Furthermore, a longer time period is required

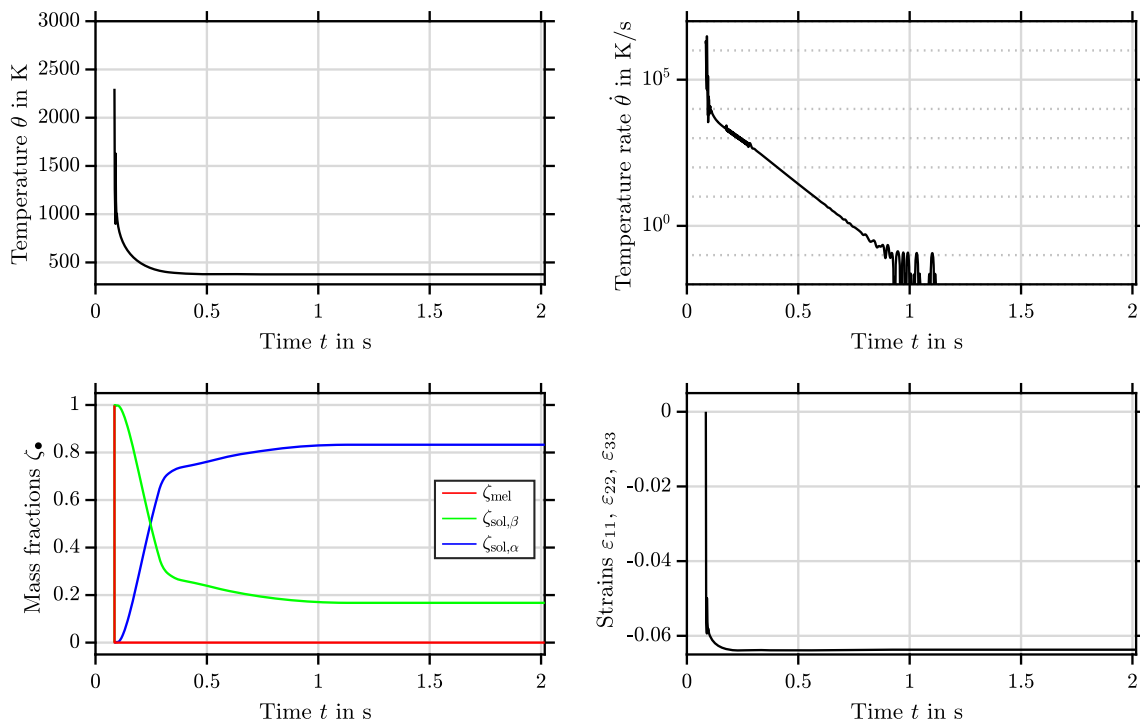


Fig. 11 Temporal evolution of homogeneous strains $\epsilon_{\bullet\bullet}$ and mass fractions ζ_i based on a prescribed temperature profile $\bar{\theta}$ and resulting temperature rate $\dot{\bar{\theta}}$ extracted from Abaqus simulation for the centred element C, compare Fig. 10

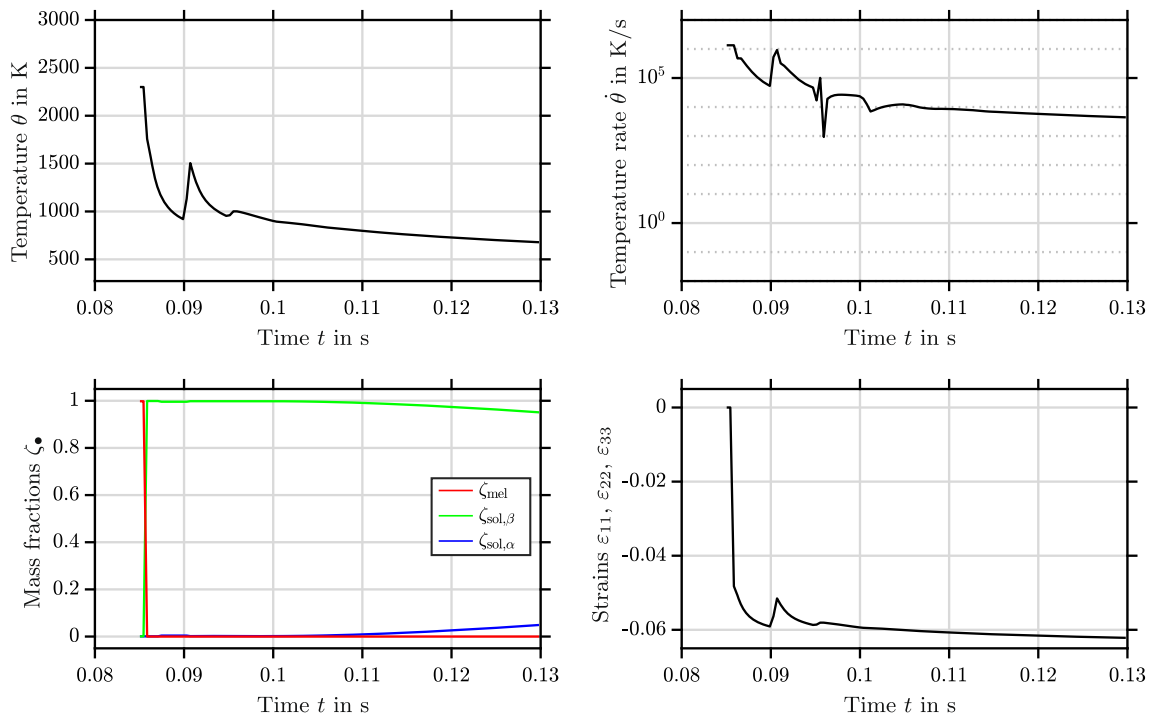


Fig. 12 Temporal evolution of homogeneous strains $\epsilon_{\bullet\bullet}$ and mass fractions ζ_i at the beginning of the prescribed $\bar{\theta}$ temperature profile and temperature rate $\dot{\bar{\theta}}$ illustrated in Fig. 11

until a phase change from both molten \rightarrow solid- β and solid- $\beta \rightarrow$ solid- α is completed. Overall, this qualitatively corre-

sponds to the expected physical behaviour of the titanium aluminium alloy. Due to the maximum constraint in eq. (37),

Table 4 Final solid- α (martensite) fraction of different elements as indicated in Fig. 10

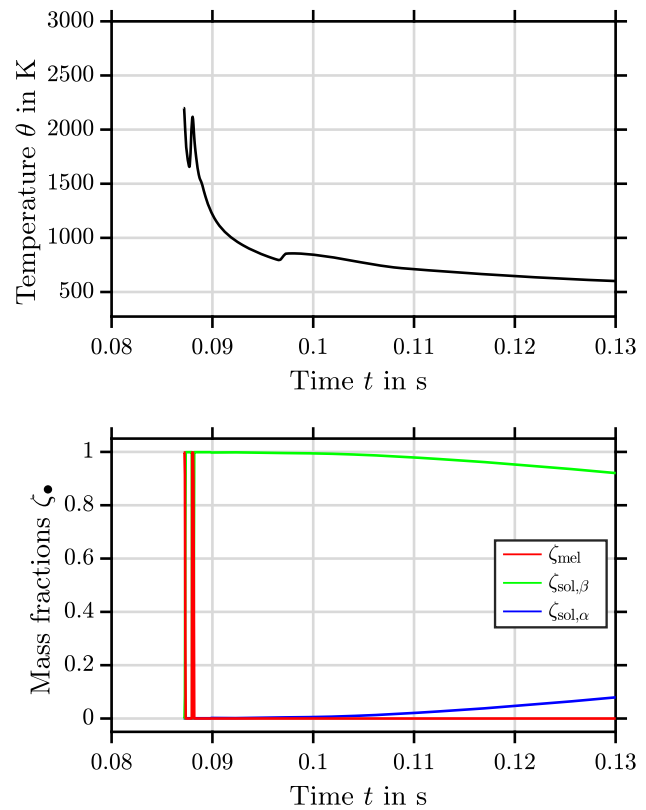
Position	Label	α -concentration $\zeta_{\text{sol}}^{\alpha}$
Top, centre	A	0.84072
Middle, left	B	0.81728
Middle, centre	C	0.83268
Middle, right	D	0.81435
Bottom, centre	E	0.71600

a portion of solid- β remains for the temperature profiles prescribed in Fig. 9a even for the complete transformation. For the higher end-temperature in Fig. 9b no complete phase change from solid- β to solid- α is obtained, but a phase mixture exists. This corresponds to the findings in e.g. [44], where different final temperatures, which - in view of PBF-LB processes - may refer to different base plate temperatures, have been evaluated. The base plate temperature highly influences the final percentage of solid- α and solid- β . The middle graph depicts the evolution of the corresponding strain state. Here, especially the jump during the phase transformation from molten to solid due to the transformation strains is visible. Furthermore, an increase of strains takes place as long as the temperature decreases due to the thermal strain contribution. Once the temperature is constant, the strains do not further evolve. In summary, the model is capable of predicting physically meaningful results not only based on different temperature rates, but also based on the final temperature.

4.3.2 Real process-based example

For the real process-based example, a simulation of a scan island with 5×5 mm is used as a basis to extract the respective temperature profiles. Details of the scan island simulation with the respective material model are described in [46, 47]. An illustration of the underlying simulation is given in Fig. 10. The results which are based on the stress-free driver introduced in Sect. 3.2 are shown in Fig. 11 for the centred element C of the scan island, as indicated in Fig. 10.

For the example, the transformation considered begins in the molten phase (not powder phase), where the current temperature is above the melting point, i.e. $\theta^{\text{melt}} = 1873.15$ K, and the initial mass fraction is set to $\zeta_{\text{mel}} = 1$. The prescribed temperature profile, the resulting temperature rate, the calculated homogeneous strain evolution and the determined distribution of the mass fractions are illustrated in Fig. 11, where the detailed temperature history and resulting evolution at the beginning is pictured in Fig. 12. The temperature rapidly decreases to $\theta < 1000$ K, where the characteristic high cooling rates present in PBF-LB processes are also recognisable. Due to the high cooling rates and the identified material parameters, an instantaneous transition from


Fig. 13 Detail of temporal evolution of mass fractions ζ_{\bullet} based on a prescribed temperature profile $\bar{\theta}$ extracted from Abaqus simulation for element B, compare Fig. 10

molten to solid- β occurs. This corresponds to a jump in the strain state. Solid- β then almost linearly decreases while solid- α simultaneously increases until $t \approx 0.3$ s, compare Fig. 11. In addition, the temperature rate decreases almost linearly until $t = 1$ s. The oscillations in the temperature rate are computational artefacts due to the temperature import from Abaqus associated with the small time steps in Matlab and are pronounced by the logarithmic scale. After the first rapid cooling, the temperature is below the martensitic start temperature $M_s \approx 820$ K, compare Fig. 8. This particular martensitic start temperature is the consequence of the simulations and occurs for all high cooling rates $\dot{\theta} > 400$ K/s. This choice seems reasonable, as M_s is reported to remain rather constant for high cooling rates in experimental work. The kinks in the evolution of mass fractions at $t \approx 0.3$ s occur due to the constantly decreasing cooling rate and increasing M_s temperature, as $\dot{\theta} < 400$ K/s is now valid. In consequence, the transformation of the remaining mass fraction takes place slower. The conversion reaches a plateau at $t = 1$ s with $\zeta_{\text{sol}}^{\alpha} = 0.83$ and, in consequence, $\zeta_{\text{sol}}^{\beta} = 0.17$, where $\dot{\theta} < 0.01$ K/s. This is supported in [25, 39], where a small solid- β fraction is present for low cooling rates. A similar curve is shown in [16], where the authors discuss

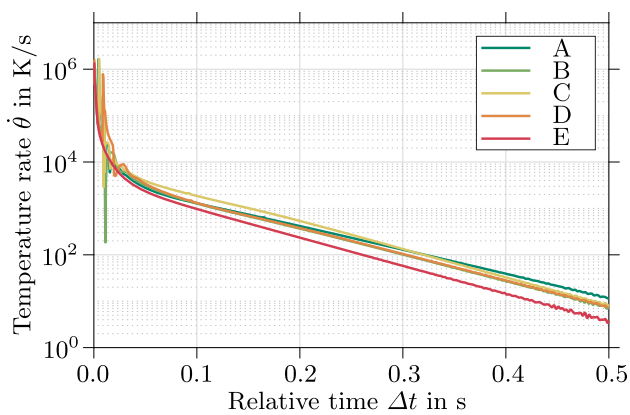


Fig. 14 Temperature rate $\dot{\theta}$ in dependence of relative cooling time Δt of all elements indicated in Fig. 10, where $\Delta t = 0$ corresponds to the specific time at which the laser beam has induced the highest temperature

the influence of neighbouring scan tracks and of inter-track idle time on the microstructure of a low-temperature transformation alloy during and at the end of the process using the KM equation. With idle-time, a complete transformation is enforced, while a small amount of solid- β is present for the standard process. The temperature cycles, i.e. heat treatment and cooling rate, not only influence the phase composition and structure, but also the hardness of the part, cf. the experimental studies in e.g. [21, 28, 42]. An analogous material behaviour can be observed in the experimental investigations in [29] where the material has been melted and reheated with decreasing laser power. This results in different temperature levels and, accordingly, the phase composition changes, which has been measured by a diffractometer. Similarly, different temperature profiles are prescribed in the simulations elaborated in [62], which result in different solid phase fractions and evolution.

In Table 4, final $\zeta_{\text{sol}}^{\alpha}$ concentrations for different elements, as indicated in Fig. 10, are summarised. Due to the different cooling rates as visualised in Figure 14, the value of $\zeta_{\text{sol}}^{\alpha}$ varies considerably. As the scan island is surrounded by powder material, heat conduction is different for all elements at the boundary of the scan island. Furthermore, no additional laser pass is present for the bottom element E, resulting in a slightly shorter cooling period and thus a considerably lower $\zeta_{\text{sol}}^{\alpha}$ value. Re-melting arises for the left and right elements B and D, as the laser beam changes the direction at the end of the scan island. Therefore, the subsequent laser pass of the neighbouring scan track results in a re-melting of these elements as visualised in Fig. 13 for element B. These elements B and D have also very similar cooling rates, compare Fig. 14. Overall, the visualised differences in the cooling rates explain the changing final mass concentration, where a low cooling rate results in small α_{sol} (element E) and high cooling rates in high α_{sol} (elements A and C) concentrations. Altogether, the

typical characteristics of an PBF-LB process are captured, including re-melting and different heating and cooling rates due to neighbouring laser scan tracks. In conclusion, from a physics viewpoint the model proposed at least qualitatively correctly captures the material properties.

5 Conclusions

A melt-solid-solid phase transformation model is proposed and applied to Ti₆Al₄V to explicitly capture the material behaviour of the molten, β - and α -phases of this material as well as combinations thereof. This is of importance as the composition of the crystal structure and material properties vary for the different phases. In consequence, the prediction of eigenstrains and eigenstresses can significantly be improved. The thermodynamically consistent and thermo-mechanically coupled framework is based on phase energy densities, where a non-standard dissipation function is used to calibrate the model to experimental data in terms of a CCT diagram. With this, a model-based CCT diagram can be implemented that consistently reflects available literature data. Therefore, only a limited number of experiments is necessary to determine the coefficients of the introduced dissipation function. Once these parameters are fitted in dependence of the present cooling rate, the remaining data, which is necessary for the dissipation function, is interpolated. The modelling and prediction of the evolution of the underlying strain contributions in addition to the microstructure composition can be considered physically plausible since a thermodynamically consistent and fully thermo-mechanically coupled phase transformation approach is used. The proposed framework is applied to the elaboration of academically chosen examples as well as real process-based PBF-LB temperature profiles extracted from Abaqus simulations. The simulations yield physically meaningful results in view of, e.g., strains and phase fraction evolution of the underlying microstructure. The modelling and simulation framework proposed can straightforwardly be applied to different process parameters during PBF-LB processes which is of significant advantage since related experimental investigations are typically expensive and time consuming.

As the absolute values of the characteristic temperatures during cooling differ in the experimental results of [5, 19, 25], it is not entirely clear which characteristic temperatures for M_s and $\theta_{\beta,\text{trans}}$ should be chosen, cf. Tables 1 and 2. However, the proposed framework can straightforwardly be adapted to different CCT data not only of this alloy, but can also be applied to other materials. If other literature data is used as a basis, different material parameters κ would be identified by the PI, resulting in, e.g., higher martensite start temperatures as found in [19, 25].

Developing different extensions of the model at hand are planned for future work. For example, a more complex material model for each phase can be incorporated in the framework, cf. previous works as [45, 46], where viscous and (visco)plastic strain contributions model the different inelastic effects of the molten and solid phase. The incorporation of an explicit transformation strain between the β - and α -phase transformation should be further evaluated, see e.g. [22, 23]. A further differentiation into α' (martensite), solid- α and solid- β and combinations thereof is one of the main future objectives and can be conducted in a straightforward manner with the proposed homogenisation approach. An overview of material behaviour and physical characteristics in the literature is given in [10], which could be used to include temperature-dependent material properties for the underlying thermal and mechanical material parameters of the α - and β -phases in order to quantitatively improve the results. As the framework is generally applicable and derived from energy densities, it can straightforwardly be transferred and adapted to other materials which possess multiple solid phases. Finally, a coupling and implementation with the previously developed multiscale model using the inherent strain method, cf. [47], into the commercial FE program Abaqus [1] is of utmost interest. With such an FE approach, the influence of the scan pattern on the composition and structure of the part—as well as the process-induced distortion and residual stresses during and at the end of the processes—can be examined, cf. the experimental findings in e.g. [32]. Possible future applications are for example the investigation of other AM processes, such as directed energy deposition (DED) where the cooling rates strongly vary due to larger melt pools, cf. [16, 61], and the examination of subsequent heat treatments, compare Fig. 2b.

Appendix

A calculation of temperature profiles

As the current framework as well as the model introduced in [44] is based on the experimental data generated in [5], the same ansatz as in [44] is used in the present work to generate the temperature curves. This means that the current temperature at position x and time t is defined via

$$\theta(x, t) = [\theta_\infty - \theta_0][f_{\text{erfc1}}(x, t) - a f_{\text{erfc2}}(x, g, t)] + \theta_0 \tag{46}$$

with

$$a = \exp(g x + g^2 \alpha t), \tag{47}$$

$$f_{\text{erfc1}}(x, t) = \text{erfc}\left(\frac{x}{2\sqrt{\alpha t}}\right), \tag{48}$$

$$f_{\text{erfc2}}(x, g, t) = \text{erfc}\left(\frac{x}{2\sqrt{\alpha t}} + g\sqrt{\alpha t}\right). \tag{49}$$

Here, erfc refers to the complementary error function, which includes several (so far) unknown parameters. Motivated by the experimental investigations in [4], the following parameters are used in the present work: $\theta_0 = 1323$ K, which denotes the temperature of the solid at the beginning of the experiment, and $\theta_\infty = 293.15$ K, representing the temperature of the cooling fluid. The position parameter is set to $x = 3.2$ mm. The material parameter α defines the thermal diffusivity and is set to $\alpha = 10$ mm²/s. Finally, the material related scalar g defines the ratio of convective heat transfer and thermal conductivity and is determined based on the current temperature θ and a quadratic ansatz so that

$$g(\theta) = s_g \left[a_g + b_g \frac{\theta - \theta_\infty}{\theta_\infty} + c_g \left[\frac{\theta - \theta_\infty}{\theta_\infty} \right]^2 \right]. \tag{50}$$

The parameters $[a_g, b_g, c_g] = [73.8, -39.3, 6.3]$ m⁻¹ have inversely been identified in [44] and s_g is introduced as a scaling parameter to generate arbitrary cooling curves. In order to generate the temperature profiles in Fig. 5, the following values are used for the scaling parameter s_g , i.e.

$$s_g = \{0.01, 0.029, 0.045, 0.134, 0.225, 0.29, 0.7, 1.19, 2.05, 2.47, 2.87, 6.38, 8.44, 17.69, 30.2, 50.8, 83.9, 125\}. \tag{51}$$

Author Contributions Conceptualization: Isabelle Noll, Thorsten Bartel, Andreas Menzel; Methodology: Isabelle Noll, Thorsten Bartel; Formal analysis and investigation: Isabelle Noll; Writing - original draft preparation: Isabelle Noll, Thorsten Bartel; Writing - review and editing: Andreas Menzel; Supervision: Andreas Menzel.

Funding Open Access funding enabled and organized by Projekt DEAL.

Declarations

Conflict of interest The authors declare that they have no conflict of interest of any nature.

Ethical approval Not applicable.

Open Access This article is licensed under a Creative Commons Attribution 4.0 International License, which permits use, sharing, adaptation, distribution and reproduction in any medium or format, as long as you give appropriate credit to the original author(s) and the source, provide a link to the Creative Commons licence, and indicate if changes were made. The images or other third party material in this article are included in the article's Creative Commons licence, unless indicated otherwise in a credit line to the material. If material is not included in the article's Creative Commons licence and your intended use is not permitted by statutory regulation or exceeds the

permitted use, you will need to obtain permission directly from the copyright holder. To view a copy of this licence, visit <http://creativecommons.org/licenses/by/4.0/>.

References

1. Abaqus: Documentation, Version 2021. Dassault Systèmes, Simulia Corp, United States (2021)
2. Additive Fertigung - Konstruktion - Teil 1: Laserbasierte Pulverbettfusion von Metallen (ISO/ASTM 52911-1:2019); Deutsche Fassung EN ISO/ASTM 52911-1:2019. Standard, Beuth Verlag GmbH (2020). <https://doi.org/10.31030/3060962>
3. Ahluwalia R, Laskowski R, Ng N, Wong M, Quek SS, Wu DT (2020) Phase field simulation of α/β microstructure in titanium alloy welds. *Mater Res Express* 7(4):046517. <https://doi.org/10.1088/2053-1591/ab875a>
4. Ahmad B, van der Veen S, Fitzpatrick M, Guo H (2018) Residual stress evaluation in selective-laser-melting additively manufactured titanium (Ti-6Al-4V) and inconel 718 using the contour method and numerical simulation. *Addit Manuf* 22:571–582. <https://doi.org/10.1016/j.addma.2018.06.002>
5. Ahmed T, Rack H (1998) Phase transformations during cooling in $\alpha + \beta$ titanium alloys. *Mater Sci Eng A* 243(1–2):206–211. [https://doi.org/10.1016/S0921-5093\(97\)00802-2](https://doi.org/10.1016/S0921-5093(97)00802-2)
6. Avrami M (1939) Kinetics of phase change. I General theory. *J Chem Phys* 7(12):1103–1112. <https://doi.org/10.1063/1.1750380>
7. Bailey NS, Katinas C, Shin YC (2017) Laser direct deposition of AISI H13 tool steel powder with numerical modeling of solid phase transformation, hardness, and residual stresses. *J Mater Process Technol* 247:223–233. <https://doi.org/10.1016/j.jmatprotec.2017.04.020>
8. Bartel T, Hackl K (2009) A micromechanical model for martensitic phase-transformations in shape-memory alloys based on energy-relaxation. *Z Angew Math Mech* 89(10):792–809. <https://doi.org/10.1002/zamm.200900244>
9. Bartel T, Geuken GL, Menzel A (2021) A thermodynamically consistent modelling framework for strongly time-dependent bainitic phase transitions. *Int J Solids Struct* 232:111172. <https://doi.org/10.1016/j.ijsolstr.2021.111172>
10. Bartsch K, Herzog D, Bossen B, Emmelmann C (2021) Material modeling of Ti-6Al-4V alloy processed by laser powder bed fusion for application in macro-scale process simulation. *Mater Sci Eng, A* 814:141237. <https://doi.org/10.1016/j.msea.2021.141237>
11. Baykasoğlu C, Akyıldız O, Tunay M, To AC (2020) A process-microstructure finite element simulation framework for predicting phase transformations and microhardness for directed energy deposition of Ti6Al4V. *Addit Manuf* 35:101252. <https://doi.org/10.1016/j.addma.2020.101252>
12. Berkovich EM, Golubeva AA, Shadek EG, Tukh LK (1978) Use of methods of solving inverse problems of heat conduction to establish the coefficient of heat transfer in jet cooling. *J Eng Phys* 34(5):619–624. <https://doi.org/10.1007/BF00860863>
13. Biot MA (1965) *Mechanics of incremental deformations*. Wiley
14. Boyer R, Welsch G, Collings EW (1994) *Materials properties handbook: titanium alloys*, 4, printing. Materials properties handbook. ASM International, Materials Park, Ohio
15. Chen F, Yan W (2020) High-fidelity modelling of thermal stress for additive manufacturing by linking thermal-fluid and mechanical models. *Mater Des* 196:109185. <https://doi.org/10.1016/j.matdes.2020.109185>
16. Chen W, Xu L, Han Y, Zhao L, Jing H (2021) Control of residual stress in metal additive manufacturing by low-temperature solid-state phase transformation: an experimental and numerical study. *Addit Manuf* 42:102016. <https://doi.org/10.1016/j.addma.2021.102016>
17. Cheon J, Na SJ (2017) Prediction of welding residual stress with real-time phase transformation by CFD thermal analysis. *Int J Mech Sci* 131:37–51. <https://doi.org/10.1016/j.ijmecsci.2017.06.046>
18. Chirurgische Implantate - Metallische Werkstoffe- Teil 3: Titan 6-Aluminium 4-Vanadium Knetlegierung (ISO 5832-3:2021); Deutsche Fassung EN ISO 5832-3:2021. Standard, Beuth Verlag GmbH (2022). <https://doi.org/10.31030/3287381>
19. Dąbrowski R (2011) The kinetics of phase transformations during continuous cooling of the Ti6Al4V alloy from the single-phase β range. *Arch Metall Mater* 56(3):703–707. <https://doi.org/10.2478/v10172-011-0077-x>
20. Dai K, Shaw L (2005) Finite element analysis of the effect of volume shrinkage during laser densification. *Acta Mater* 53(18):4743–4754. <https://doi.org/10.1016/j.actamat.2005.06.014>
21. Davids WJ, Chen H, Nomoto K, Wang H, Babu S, Primig S, Liao X, Breen A, Ringer SP (2021) Phase transformation pathways in Ti-6Al-4V manufactured via electron beam powder bed fusion. *Acta Mater* 215:117131. <https://doi.org/10.1016/j.actamat.2021.117131>
22. De Baere D, Bayat M, Mohanty S, Hattel JH (2020) Part-scale mechanical modelling of LPBF including microstructural evolution effects. *IOP Conf. Ser.: Mater. Sci. Eng.* 861(1):012013. <https://doi.org/10.1088/1757-899X/861/1/012013>
23. DebRoy T, Wei HL, Zuback JS, Mukherjee T, Elmer JW, Milewski JO, Beese AM, Wilson-Heid A, De A, Zhang W (2018) Additive manufacturing of metallic components—process, structure and properties. *Prog Mater Sci* 92:112–224. <https://doi.org/10.1016/j.pmatsci.2017.10.001>
24. Fang J, Dong S, Wang Y, Xu B, Zhang Z, Xia D, He P (2015) The effects of solid-state phase transformation upon stress evolution in laser metal powder deposition. *Mater Des* 87:807–814. <https://doi.org/10.1016/j.matdes.2015.08.061>
25. Janda A, Ebenbauer S, Prestl A, Siller I, Clemens H (2022) Microstructural adjustment of hot-rolled Ti-6Al-4V based on a CCT diagram. *Mater Sci Technol* 38(13):957–964. <https://doi.org/10.1080/02670836.2022.2068243>
26. Johnson W, Mehl R (1939) Reaction kinetics in processes of nucleation and growth. *Trans Metall Soc AIME* 135:416–442
27. Junker P, Hackl K (2011) Finite element simulations of polycrystalline shape memory alloys based on a micromechanical model. *Comput Mech* 47(5):505–517. <https://doi.org/10.1007/s00466-010-0555-4>
28. Kaschel F, Vijayaraghavan R, Shmeliov A, McCarthy E, Canavan M, McNally P, Dowling D, Nicolosi V, Celikin M (2020) Mechanism of stress relaxation and phase transformation in additively manufactured Ti-6Al-4V via in situ high temperature XRD and TEM analyses. *Acta Mater* 188:720–732. <https://doi.org/10.1016/j.actamat.2020.02.056>
29. Kenel C, Grolimund D, Li X, Panepucci E, Samson VA, Sanchez DF, Marone F, Leinenbach C (2017) In situ investigation of phase transformations in Ti-6Al-4V under additive manufacturing conditions combining laser melting and high-speed micro-X-ray diffraction. *Sci Rep* 7(1):16358. <https://doi.org/10.1038/s41598-017-16760-0>
30. Koistinen D, Marburger R (1959) A general equation prescribing the extent of the austenite-martensite transformation in pure iron-carbon alloys and plain carbon steels. *Acta Metall* 7(1):59–60. [https://doi.org/10.1016/0001-6160\(59\)90170-1](https://doi.org/10.1016/0001-6160(59)90170-1)
31. Kolmogorov AN (1937) On the statistical theory of metal crystallization. *Bull Acad Sci USSR Math Ser* 1:335–359
32. Kumar P, Prakash O, Ramamurthy U (2018) Micro-and meso-structures and their influence on mechanical properties of selectively laser melted Ti-6Al-4V. *Acta Mater* 154:246–260. <https://doi.org/10.1016/j.actamat.2018.05.044>

33. Leyens C, Peters M (eds) (2003) Titanium and titanium alloys: fundamentals and applications. Wiley, Weinheim. <https://doi.org/10.1002/3527602119>
34. Liang Z, Sun Z, Zhang W, Wu S, Chang H (2019) The effect of heat treatment on microstructure evolution and tensile properties of selective laser melted Ti6Al4V alloy. *J Alloy Compd* 782:1041–1048. <https://doi.org/10.1016/j.jallcom.2018.12.051>
35. Lindroos M, Pinomaa T, Antikainen A, Lagerbom J, Reijonen J, Lindroos T, Andersson T, Laukkanen A (2021) Micromechanical modeling approach to single track deformation, phase transformation and residual stress evolution during selective laser melting using crystal plasticity. *Addit Manuf* 38:101819. <https://doi.org/10.1016/j.addma.2020.101819>
36. Liu S, Shin YC (2020) Prediction of 3D microstructure and phase distributions of Ti6Al4V built by the directed energy deposition process via combined multi-physics models. *Addit Manuf* 34:101234. <https://doi.org/10.1016/j.addma.2020.101234>
37. Lu H, Deng W, Luo K, Chen Y, Wang J, Lu J (2023) Tailoring microstructure of additively manufactured Ti6Al4V titanium alloy using hybrid additive manufacturing technology. *Addit Manuf* 63:103416. <https://doi.org/10.1016/j.addma.2023.103416>
38. Mahnken R, Stein E (1997) Parameter identification for finite deformation elasto-plasticity in principal directions. *Comput Methods Appl Mech Eng* 147(1–2):17–39. [https://doi.org/10.1016/S0045-7825\(97\)00008-X](https://doi.org/10.1016/S0045-7825(97)00008-X)
39. Malinov S, Guo Z, Sha W, Wilson A (2001) Differential scanning calorimetry study and computer modeling of $\beta \rightarrow \alpha$ phase transformation in a Ti–6Al–4V alloy. *Metall Mater Trans A* 32(4):879–887. <https://doi.org/10.1007/s11661-001-0345-x>
40. Meier C, Penny RW, Zou Y, Gibbs JS, Hart AJ (2017) Thermophysical phenomena in metal additive manufacturing by selective laser melting: fundamentals, modeling, simulation and experimentation. *Annu Rev Heat Transfer* 20:241–316. <https://doi.org/10.1615/AnnualRevHeatTransfer.2018019042>
41. Mills K (2002) Recommended values of thermophysical properties for selected commercial alloys. Woodhead Publishing
42. Muhammad M, Pegues JW, Shamsaei N, Haghshenas M (2019) Effect of heat treatments on microstructure/small-scale properties of additive manufactured Ti–6Al–4V. *Int J Adv Manuf Technol* 103(9–12):4161–4172. <https://doi.org/10.1007/s00170-019-03789-w>
43. Nie P, Ojo O, Li Z (2014) Numerical modeling of microstructure evolution during laser additive manufacturing of a nickel-based superalloy. *Acta Mater* 77:85–95. <https://doi.org/10.1016/j.actamat.2014.05.039>
44. Nitzler J, Meier C, Müller KW, Wall WA, Hodge NE (2021) A novel physics-based and data-supported microstructure model for part-scale simulation of laser powder bed fusion of Ti–6Al–4V. *Adv Model Simul Eng Sci* 8(1):16. <https://doi.org/10.1186/s40323-021-00201-9>
45. Noll I, Bartel T, Menzel A (2020) A computational phase transformation model for selective laser melting processes. *Comput Mech* 66:1321–1342. <https://doi.org/10.1007/s00466-020-01903-4>
46. Noll I, Bartel T, Menzel A (2021) On the incorporation of a micromechanical material model into the inherent strain method: application to the modeling of selective laser melting. *GAMM-Mitteilungen* 44(3):e202100015. <https://doi.org/10.1002/gamm.202100015>
47. Noll I, Koppka L, Bartel T, Menzel A (2022) A micromechanically motivated multiscale approach for residual distortion in laser powder bed fusion processes. *Addit Manuf* 60:103277. <https://doi.org/10.1016/j.addma.2022.103277>
48. Pagano S, Alart P, Maisonneuve O (1998) Solid-solid phase transition modelling. Local and global minimizations of non-convex and relaxed potentials. Isothermal case for shape memory alloys. *Int J Eng Sci* 36(10):1143–1172. [https://doi.org/10.1016/S0020-7225\(98\)00010-X](https://doi.org/10.1016/S0020-7225(98)00010-X)
49. Pal S, Gubeljak N, Hudák R, Lojen G, Rajtúková V, Brajlíh T, Drstvenšek I (2020) Evolution of the metallurgical properties of Ti–6Al–4V, produced with different laser processing parameters, at constant energy density in selective laser melting. *Results Phys* 17:103186. <https://doi.org/10.1016/j.rinp.2020.103186>
50. Pederson R, Babushkin O, Skystedt F, Warren R (2003) Use of high temperature X-ray diffractometry to study phase transitions and thermal expansion properties in Ti–6Al–4V. *Mater Sci Technol* 19(11):1533–1538. <https://doi.org/10.1179/026708303225008013>
51. Smith J, Xiong W, Cao J, Liu WK (2016) Thermodynamically consistent microstructure prediction of additively manufactured materials. *Comput Mech* 57(3):359–370. <https://doi.org/10.1007/s00466-015-1243-1>
52. Sun D, Gu D, Lin K, Ma J, Chen W, Huang J, Sun X, Chu M (2019) Selective laser melting of titanium parts: Influence of laser process parameters on macro- and microstructures and tensile property. *Powder Technol* 342:371–379. <https://doi.org/10.1016/j.powtec.2018.09.090>
53. Teuindjang JT, Paydas H, Tran HS, Carrus R, Duchêne L, Mertens A, Habraken AM (2021) A new concept for modeling phase transformations in Ti6Al4V alloy manufactured by directed energy deposition. *Materials* 14(11):2985. <https://doi.org/10.3390/ma14112985>
54. Teixeira J, Maréchal D, Wimpory R, Denis S, Lefebvre F, Frappier R (2022) Formation of residual stresses during quenching of Ti17 and Ti–6Al–4V alloys: influence of phase transformations. *Mater Sci Eng A* 832:142456. <https://doi.org/10.1016/j.msea.2021.142456>
55. Vastola G, Zhang G, Pei QX, Zhang YW (2016) Modeling the microstructure evolution during additive manufacturing of Ti6Al4V: a comparison between electron beam melting and selective laser melting. *J Miner Met Mater Soc* 68(5):1370–1375. <https://doi.org/10.1007/s11837-016-1890-5>
56. Wang H, Chao Q, Chen H, Chen Z, Primig S, Xu W, Ringer S, Liao X (2022) Formation of a transition V-rich structure during the α' to $\alpha + \beta$ phase transformation process in additively manufactured Ti–6Al–4V. *Acta Mater* 235:118104. <https://doi.org/10.1016/j.actamat.2022.118104>
57. Yadroitsev I, Krakhmalev P, Yadroitsava I (2014) Selective laser melting of Ti6Al4V alloy for biomedical applications: temperature monitoring and microstructural evolution. *J Alloy Compd* 583:404–409. <https://doi.org/10.1016/j.jallcom.2013.08.183>
58. Yang Y, Jamshidinia M, Boulware P, Kelly S (2018) Prediction of microstructure, residual stress, and deformation in laser powder bed fusion process. *Comput Mech* 61(5):599–615. <https://doi.org/10.1007/s00466-017-1528-7>
59. Yang X, Barrett RA, Tong M, Harrison NM, Leen SB (2021) Towards a process-structure model for Ti–6Al–4V during additive manufacturing. *J Manuf Process* 61:428–439. <https://doi.org/10.1016/j.jmapro.2020.11.033>
60. Yi M, Xu BX, Gutfleisch O (2019) Computational study on microstructure evolution and magnetic property of laser additively manufactured magnetic materials. *Comput Mech* 64(4):917–935. <https://doi.org/10.1007/s00466-019-01687-2>
61. Zhai Y, Galarraga H, Lados D (2016) Microstructure, static properties, and fatigue crack growth mechanisms in Ti–6Al–4V fabricated by additive manufacturing: LENS and EBM. *Eng Fail Anal* 69:3–14. <https://doi.org/10.1016/j.engfailanal.2016.05.036>
62. Zhang Q, Xie J, Gao Z, London T, Griffiths D, Oancea V (2019) A metallurgical phase transformation framework applied to SLM additive manufacturing processes. *Mater Des* 166:107618. <https://doi.org/10.1016/j.matdes.2019.107618>

Publisher's Note Springer Nature remains neutral with regard to jurisdictional claims in published maps and institutional affiliations.